



TECHNISCHE  
UNIVERSITÄT  
WIEN

GREGOR SCHESTAK, BSc.

# Simulation and Measurement of a MEMS Resonant Displacement Sensor

**Master Thesis**

to achieve the university degree of

Master of Science

Master's degree programme: Microelectronics and Photonics

submitted to

**Vienna University of Technology**

Supervisor

DI. Alexander Dabsch

Institute of Sensor and Actuator Systems  
Ao. Univ.Prof. Dipl.-Ing. Dr.techn. Franz Keplinger

Vienna, January 2019

This document is set in Palatino, compiled with [pdfL<sup>A</sup>T<sub>E</sub>X2<sub>ε</sub>](#) and [Biber](#).

The L<sup>A</sup>T<sub>E</sub>X template from Karl Voit is based on [KOMA script](#) and can be found online:  
<https://github.com/novoid/LaTeX-KOMA-template>

## Affidavit

Hiermit erkläre ich, dass die vorliegende Arbeit gemäß Code of Conduct – Regeln zur Sicherung guter wissenschaftlicher Praxis (in der aktuellen Fassung des jeweiligen Mitteilungsblattes der TU Wien), insbesondere ohne unzulässige Hilfe Dritter und ohne Benutzung anderer als der angegebenen Hilfsmittel, angefertigt wurde. Die aus anderen Quellen direkt oder indirekt übernommenen Daten und Konzepte sind unter Angabe der Quelle gekennzeichnet. Die Arbeit wurde bisher weder im In- noch im Ausland in gleicher oder in ähnlicher Form in anderen Prüfungsverfahren vorgelegt.

---

Datum

---

Unterschrift



# Abstract

MEMS technology is still a growing economy, as it has many advantages in building complex sensors due to its small and compact dimensions. A resonator is a special type of structure which is used in the MEMS world very often. Because of the small design the resonance frequency depends a lot on the external influence on the sensor structure or the change of its environment. For this master thesis a resonator is expected to be sensitive to displacement from its out-of-plane axis. For this purpose a new design was developed and simulated and compared to a fabricated, second design, working under similar conditions. For the confirmation of this thesis the alternative design had to be constructed and measured. This thesis is therefore subdivided to the major part simulation and then the fabrication, excitation and measurement of a second sensor.



# Kurzfassung

Der Markt der MEMS Technologien ist immer noch stark im Wachstum. Einer der Gründe dafür ist die Möglichkeit komplexe Sensorik in immer kompakterer Bauform entwickeln zu können. Ein resonanter Sensor ist ein spezieller Typ, welcher sich gut mit MEMS Technologien umsetzen lässt. Aufgrund der kleinen Dimension und hoher Güte dieser Sensoren wirken sich äußere Einwirkungen auf die Sensorstruktur und Änderungen auf die Umgebung stark aus, wodurch sich auch die Resonanzfrequenz des Sensors relativ stark verändert. Im Fall dieser Diplomarbeit sollte sich die Resonanzfrequenz aufgrund einer Verschiebung in der Achse, welche normal zur Sensorebene steht, soweit verändern, dass man daraus auf die Verschiebung schließen kann. Hierfür wurde ein neues Design entwickelt und simuliert. Zum Vergleich wurde ein zweites, fertiges Design ebenfalls in einem ähnlichem Umfeld analysiert. Zur Bestätigung der Simulation, wurde dieser alternative Sensor in einem speziellen Messaufbau vermessen. Die Arbeit teilt sich daher in den großen Hauptteil Simulation, sowie Aufbau, Anregung und Vermessung des alternativen Sensors.



# Nomenclature

## Abbreviation

AFM Atomic Force Microscopy

DETF Double Ending Tuning Fork

EMD Electro Magnetic Drive

FEM Finite Element Model

ISAS Institute for Sensors and Actuator Systems

LDV Laser-Doppler-Vibrometer

MEMS Microelectromechanical Systems

MSA Micro Systems Analyzer

NEMS Nanoelectromechanical Systems

PRE Piezo Resistive Effect

SCR Stress Concentration Regions

SNR Signal to Noise Ratio

## Variables

$\omega$	Angular Frequency	$s^{-1}$
$\Omega_n$	Eigenfrequency	Hz
$\Omega_R$	Resonance Frequency	Hz
$\rho$	Density	$kg/m^3$
$A$	Area	$m^2$
$E$	Young's modulus	GPa
$F_N$	Normal Force	N
$F_Q$	Shear Force	N
$h$	Structure Height	m
$I$	Moment of Inertia	$kg \cdot m^2$
$k$	Spring Constant	N/m
$l$	Beam Length	m
$M_b$	Bending Moment	Nm
$q$	Load	N
$u(x, t)$	Vibration Shape	$m \cdot s$
$w$	Beam Width	m
$z$	Displacement	m

# Contents

<b>Abstract</b>	<b>v</b>
<b>1 Basic Principle of Resonant Sensors</b>	<b>1</b>
1.1 Sensor characteristics	2
1.1.1 Responsivity	2
1.1.2 Sensitivity	3
1.1.3 Response Time	3
1.1.4 Q factor	4
1.2 Beam Theory	5
1.3 Analytical Model	9
1.4 Lumped-Element Model Resonator	14
1.5 Summarized Fabrication Process	14
<b>2 Simulations</b>	<b>17</b>
2.1 Simulation Setup	17
2.2 Model Implementation and Development	18
2.2.1 Initial Point	20
2.2.2 Parameter Variation	20
2.3 Final Design	32
2.3.1 Fabricated Sensor	34
<b>3 Readout</b>	<b>37</b>
3.1 Piezo-resistive Readout	38
3.1.1 Wheatstone Bridge	39

## Contents

3.2	Optical Readout . . . . .	42
3.3	Piezoelectric Layer Readout . . . . .	44
<b>4</b>	<b>Excitation</b>	<b>45</b>
4.1	Lorentz force . . . . .	45
4.2	Piezo-electric . . . . .	47
<b>5</b>	<b>Measurement</b>	<b>49</b>
5.1	Measurement Setup . . . . .	49
5.1.1	Fixing to the Actor . . . . .	51
5.2	Results . . . . .	53
<b>6</b>	<b>Conclusion</b>	<b>57</b>
	<b>Bibliography</b>	<b>59</b>

# List of Figures

1.1	Definition of the responsivity . . . . .	3
1.2	Excursion characteristics of the final design . . . . .	5
1.3	Doubly clamped beam . . . . .	6
1.4	Doubly clamped beam, infinitesimal small part . . . . .	6
1.5	Comparison of the analytical and the FEM model . . . . .	12
1.6	Comparison of the analytical and the FEM simulation . . . . .	13
1.7	Lumped-Element Model . . . . .	15
1.8	Fabrication procesflow . . . . .	16
2.1	Simulation model . . . . .	19
2.2	Variation of the beam length . . . . .	23
2.3	Size ratio dependency of the eigenfrequency . . . . .	23
2.4	Variation of the beam width . . . . .	24
2.5	Development of the multiple beam design . . . . .	25
2.6	Simulation of the beam amount . . . . .	27
2.7	Variation of the thickness . . . . .	28
2.8	Influence of the hole in the middle . . . . .	29
2.9	Materials and their Young's modulus relation . . . . .	30
2.10	Variation of the material . . . . .	31
2.11	Final design in COMSOL . . . . .	32
2.12	Final design of the in-plane vibration . . . . .	33
2.13	Responsivity slope of the final design . . . . .	33
2.14	Fabricated design, five mechanical degrees of freedom . . . . .	35

## List of Figures

2.15	Alternative sensor simulation . . . . .	35
2.16	Sensor characteristic of the fabricated design . . . . .	36
3.1	Schematic of the Wheatstone bridge. . . . .	41
3.2	Doppler effect . . . . .	43
4.1	Lorentz force actuation . . . . .	46
4.2	Piezo-electric . . . . .	47
5.1	Bending actor . . . . .	50
5.3	Sensor on the bending actuator . . . . .	51
5.2	Measurement setup . . . . .	52
5.6	Modeshape in COMSOL for the measurement . . . . .	54
5.4	Result of the first symmetrical mode . . . . .	55
5.5	Result of the first antisymmetrical mode . . . . .	56

# 1 Basic Principle of Resonant Sensors

Resonance is a fundamental phenomenon in oscillating systems, it can and must be observed in interdisciplinary fields. We deal with it in our subconscious as we try maximizing the excursion on the swing. It is also a powerful phenomenon as it can be seen when the aeroelastic flutter matched the resonance frequency a bridge collapsed during a storm (Tacoma Narrows Bridge, 1940). We also depend on it for the sense of hearing, when hair cells react frequency selectively to acoustic waves in the cochlea [9]. One can find resonant systems everywhere, from biological cells to quantum mechanics and electronic devices, but the resonance frequency is not a universal constant, it is influenced by its environment. A fact that can be made use of, if we want to monitor this environment and measure a certain parameter. Here resonance sensors appear, one can excite a structure to oscillate in its resonance frequency and monitor its behavior to the environment. An important point is that the sensor should only react to the parameter one wants to measure, though this is not possible since it will react to every change in its environment, therefore, it should react here at least in the strongest way. There are different ways to measure these parameters through resonance change, as it is described by Oliver Brand [10].

This thesis shows one certain way to measure the displacement of a sensor. The idea is to use a structure, which is excited in resonance, and to measure the vibration frequency. A displacement in the out-of-plane direction from one side of the structure to the other side should change the resonance frequency, the shift in the phase between actuation and readout has to be detectable. The displacement should be tiny, in the low nanometer or picometer region. As a comparison one can look at an AFM (Atomic

## 1 Basic Principle of Resonant Sensors

Force Microscopy), which is able to measure these small excursion with a very unhandy optical readout. When using the AFM non contact mode a force gradient, caused by the van der Waals forces, induces a displacement which will observably shift the resonance frequency [11]. This thesis on the other hand, will focus only on the displacement and the resulting resonance shift and not on the way how this displacement is caused.

### 1.1 Sensor characteristics

In order to understand and describe the quality of a sensor one can look at certain specifications defined by Schmid [13] and Kalantar-zadeh [8]. By its responsivity, resolution, sensitivity and response time a sensor can be evaluated whether it can fulfill the requirements to measure a desired parameter.

#### 1.1.1 Responsivity

Responsivity describes the sensor output as a function of the sensor input. In other words, when the input changes the output will change as well, according to the value of the responsivity. In the linear section of the sensor's operating range, this value is constant. In the case of this thesis the responsivity is proportional to the change in eigenfrequency  $\Delta\Omega$ , which should be obviously as high as possible. Mathematically this can be described as:

$$\mathfrak{R} \approx \frac{\Delta\Omega}{\Delta\zeta} \quad (1.1)$$

with  $\Omega$  being the eigenfrequency and  $\zeta$  the displacement. Slope and Tangent are depicted in Fig. 1.1. For this thesis a minimal change of 1 Hz for 1 nm displacement is aspired.

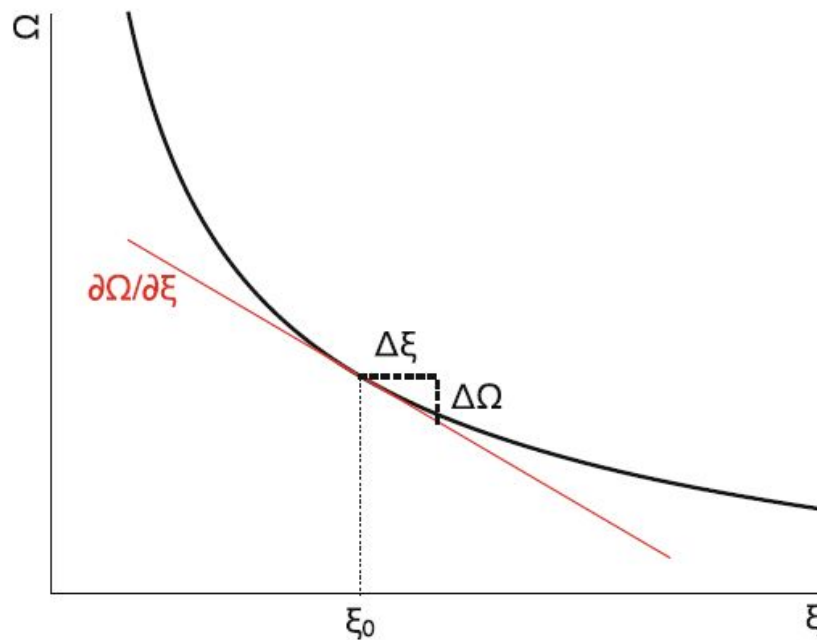


Figure 1.1: Responsivity, the slope of the tangent should be as large as possible. (Source: Schmid [13] chapter 3)

### 1.1.2 Sensitivity

Sensitivity defines the smallest detectable change of the input, it is limited by the SNR (Signal to Noise Ratio). For this thesis, the sensitivity should be less than 1 nm. The sensitivity can be different for certain operation ranges, but should be constant in a large range. It can even reach saturation, where no input change can be detected at all.

### 1.1.3 Response Time

The response time, is the period from the sudden change of the input quantity to the resulting change of the output quantity, whereas here normally 90% of the final value have to be reached. This time depends on the quality factor  $Q$  and the eigenfrequency

## 1 Basic Principle of Resonant Sensors

of the resonating structure. As it is stated in Bilal Orun and Guvenc [2], an extremely high Q factor must not be desired as the response time  $\tau$  follows Eq. 1.2,  $\omega_n$  standing for the eigenfrequency in the mode n.

$$\tau = \frac{2Q}{\omega_n} \quad (1.2)$$

### 1.1.4 Q factor

The quality factor indicates how under-damped an oscillating system is. Abdolvand [1] defines the quality factor by the ratio of the stored energy and the lost energy per cycle

$$Q \equiv 2\pi \frac{\text{energy stored}}{\text{energy disipated per cycle}} \quad (1.3)$$

At resonance the amplitude reaches its maximum. For such low damped systems the resonance frequency equals the eigenfrequency of the structure. The Q factor depends on different damping mechanism (Eq. 1.5), as it is described in Schmid [13] chapter two.  $Q_{Support}$  considers the support losses,  $Q_{Kinetic}$  the losses due to the surrounding gas and  $Q_{Intrinsic}$  intrinsic properties, like damping by material For this thesis only the air damping was considered in the COMSOL simulation, as described in Ch. 2.2. In MEMS the quality factor can reach a value of thousands and in NEMS (Nano Electro Mechanical Systems) even millions. There are some methods for calculating the Q factor, one of them being the 3 dB method. Here, the bandwidth where the amplitude is being lower than 3 dB than the maximum is divided by the resonance frequency

$$Q = \frac{\Omega_R}{\Delta\Omega_{-3dB}} \quad (1.4)$$

The characteristic of the Q factor for the final design can be seen in Fig. 1.2, where the vibration amplitude in resonance is about 80 nm in the in-plane direction. The bandwidth is approximately 0.5 Hz, here the amplitude is higher then the 3 dB limit (in this case 40 nm). After Eq. 1.4 the quality factor is 70000, the Q factor directly read from COMSOL would be 50000. The deviation could come from different

calculation methods or the influence of damping, also from an uncertain reading as the characteristic is very steep around the resonance. Furthermore, it looks like there are some inharmonic effects.

$$\frac{1}{Q_{Total}} = \left( \frac{1}{Q_{Support}} + \frac{1}{Q_{Intrinsic}} + \frac{1}{Q_{Kinetic}} + \dots \right) \quad (1.5)$$

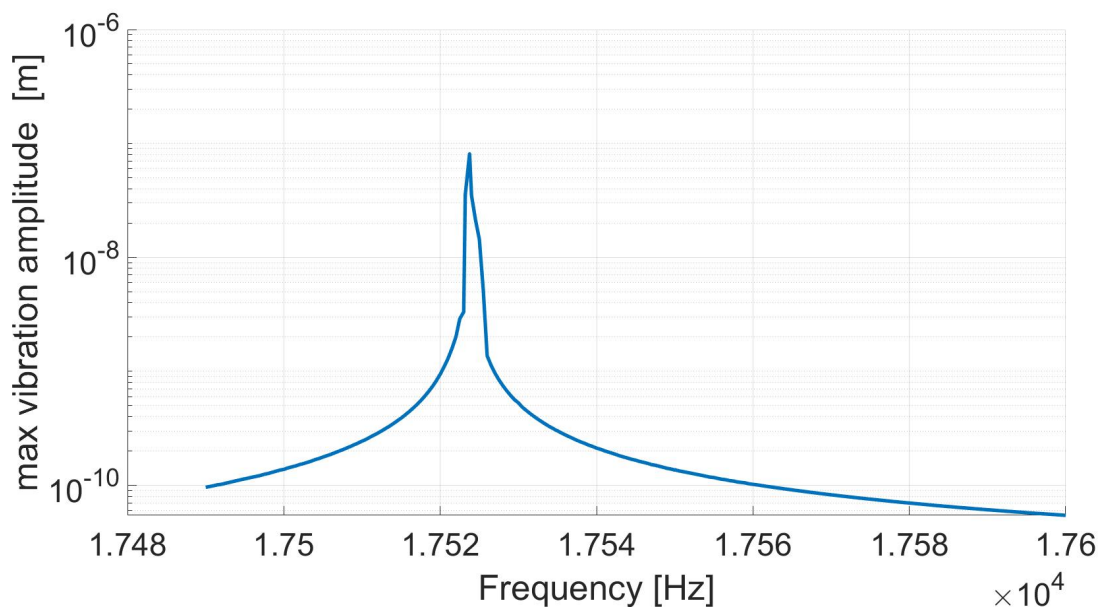


**Figure 1.2:** Vibration amplitude of the final design caused by different excitation frequencies. There is no other displacement of the structure for this simulation. Here, only airdamping is considered.

## 1.2 Beam Theory

To be able to find an appropriate design for the sensor we have to find solutions for the eigenmodes of the vibration structure. The modes can be calculated following the Euler-Bernoulli beam theory. A picture of a doubly clamped beam is shown in Fig. 1.3 with  $l$  the length of the beam,  $I_y$  moment of inertia,  $\rho$  material density,  $w(x)$  the deflection depending on the location  $x$ , and  $A$  the area of the beam's cross section.

## 1 Basic Principle of Resonant Sensors

In Fig. 1.4 one can see a differential part of the beam: With  $M_b$  the side load and  $\Delta M_b$  the differential side load,  $q$  a uniformly distributed load.

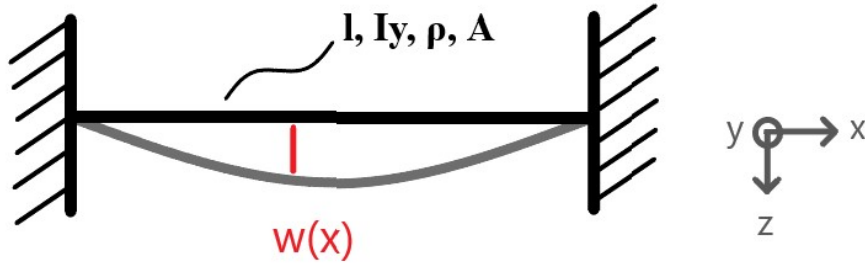


Figure 1.3: Sketch of the doubly clamped beam, as it is intended for the analytical model.

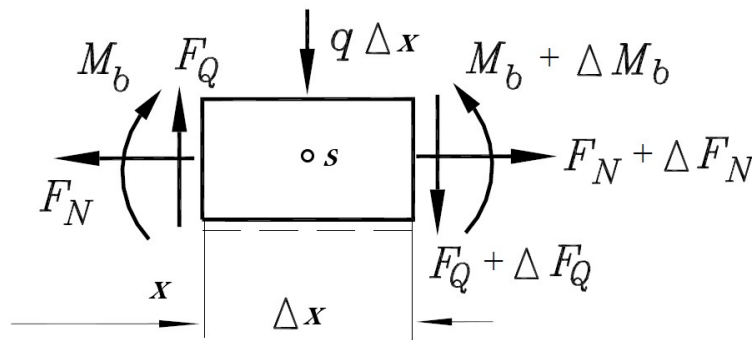


Figure 1.4: Infinitesimal small part of the doubly clamped beam (Juergen Dankert [7], chapter 7.)

The general momentum principle after [7] says that the time deviation of the total momentum from a mass-point-system equals the resulting forces from the outside. For the cross section in Fig. 1.4 this would be:

$$-F_Q + q\Delta x + F_Q + \Delta F_Q = \rho \cdot A \cdot \Delta x \cdot \frac{\partial^2 w}{\partial t^2} \quad (1.6)$$

, divided by  $\Delta$  and with  $\Delta \rightarrow 0$  the momentum principle looks like:

$$\frac{\partial F_Q}{\partial x} = \rho \cdot A \cdot \frac{\partial^2 w}{\partial x^2} - q \quad (1.7)$$

With  $s$  as the center of gravity in Fig. 1.4 one can use the angular momentum principle. In its general form it would be the time deviation of the total angular momentum from a mass-point-system, is equal to the resulting momentum on the outside. With  $L_0$  being the outside momentum:

$$-M_b - F_Q \cdot \Delta x + M_b + \frac{\partial M_b}{\partial x} \Delta x = w_y \varrho I_y \Delta x \quad (1.8)$$

The angle  $\varphi$  of the cross section is equal to the slope of the beam axis  $\partial w / \partial x$  and  $w_y = -\partial^2 w / \partial x \partial t$ . Inserting Eq. 1.8 in 1.7 and again dividing by  $\Delta$  and  $\Delta \rightarrow 0$  delivers

$$\frac{\partial M_b}{\partial x} = F_Q - \varrho \cdot I_y \cdot \frac{\partial^3 w}{\partial x \partial t^2} \quad (1.9)$$

With the differential equation of the static bending of a beam element:

$$\frac{\partial^2 w}{\partial x^2} = -\frac{M_b}{EI_y} \quad (1.10)$$

$$-\frac{\partial M_b}{\partial x} = F_Q \quad (1.11)$$

Eq. 1.7 and 1.9 are the connection between load  $q$ , shear force  $F_Q$  and the bending moment  $M_b$ . Normally, one can neglect the influence of the second term on the right hand side of Eq. 1.9, which represents the rotary inertia of the infinitesimal beam element. Differentiating 1.10 two times with respect to  $x$  and inserting  $M_b$  and  $F_Q$  from Eq. 1.11 and Eq. 1.6 we get

$$EI \frac{\partial^4 w}{\partial x^4} = q - \varrho \cdot A \cdot \frac{\partial^2 w}{\partial t^2} \quad (1.12)$$

Here, we assume, that  $I$  is independent on  $x$ . For the solution of Eq. 1.12 we assume a system without load and rewrite Eq. 1.12 to

$$c^2 \frac{\partial^4 w}{\partial x^4} + \frac{\partial^2 w}{\partial t^2} = 0 \quad (1.13)$$

with  $c^2 = \frac{EI}{\varrho A}$

## 1 Basic Principle of Resonant Sensors

For this differential equation we use the product ansatz

$$w(x, t) = f(x)g(t) \quad (1.14)$$

leading to

$$c^2 \frac{f^{IV}(x)}{f(x)} = -\frac{g''(t)}{g(t)} \quad (1.15)$$

This equation is only valid for all  $x$  and  $t$  when both terms are constant, we use  $w^2$ .

This leads to

$$g''(t) + w^2 g(t) = 0 \quad (1.16a)$$

$$f^{IV}(x) - \left(\frac{w}{c}\right)^4 f(x) = 0 \quad (1.16b)$$

with the general solutions

$$g(t) = A \cdot \cos(\omega t - \varphi) \quad (1.17a)$$

$$f(x) = a \cdot \sin(\beta x) + b \cdot \cos(\beta x) + c \cdot \sinh(\beta x) + d \cdot \cosh(\beta x) \quad (1.17b)$$

with  $\gamma = w/c$ . Now we have to consider the boundary conditions to find the constants  $a, b, c$  and  $d$ . For a double clamped beam we get

$$w(0) = w'(0) = 0 \quad (1.18a)$$

$$w(l) = w'(l) = 0 \quad (1.18b)$$

inserting to Eq. 1.17 and their derivative we yield

$$b + d = 0 \longrightarrow b = -d \quad (1.19a)$$

$$a - c = 0 \longrightarrow a = c \quad (1.19b)$$

$$a (\sinh(\beta l) - \sin(\beta l)) + b (\cosh(\beta l) - \cos(\beta l)) = 0 \quad (1.19c)$$

$$a\beta (\cosh(\beta l) - \cos(\beta l)) + b\beta (\sinh(\beta l) - \sin(\beta l)) = 0 \quad (1.19d)$$

or written in matrix form as

$$\begin{bmatrix} m_1 & m_2 \\ m_3 & m_4 \end{bmatrix} \begin{bmatrix} a \\ b \end{bmatrix} = 0 \quad (1.20)$$

This system has a nontrivial solution only if the determinate of the matrix  $M$  is zero ( $\det(M) = 0$ ) which yields finally to

$$1 - \cos(\beta l) \cdot \cosh(\beta l) = 0 \quad (1.21)$$

This transcendent equation has infinite large number of solutions, the first are  $\beta_1 l = 1.1875$ ,  $\beta_2 l = 4.694$  and  $\beta_3 l = 7.855$  which corresponds to eigenfrequencies  $w_i = c \cdot \beta^2$ .

The approximations can be calculated with the analytical model, for more complex structures a numerical model is a better option. For exact results of the more complex structures a FEM (Finite Element Method) simulation was used, which is described in chapter 2. In the analytical case only the simple beam with a mass in the middle was calculated to get an idea where the eigenfrequency of the structure will be and how it will change in regard to geometric and material modification.

A very simplified solution for a rectangular beam eigenfrequency, as it is calculated in Shengli Kong [15], will result in Eq. 1.22.

$$\Omega = (n\pi)^2 \sqrt{\frac{Eh^2}{12\rho L^4}} \quad (1.22)$$

## 1.3 Analytical Model

Now the beam theory from above can be used to create an analytical model for the design of this thesis. In Fig. 1.5a one can see an existing model from Juergen Dankert [7]. The initial structure in Fig. 1.5c has two beams and a larger middle part, this can be transformed to the analytical model. Note that the initial structure has two beams

## 1 Basic Principle of Resonant Sensors

with equal length, therefor, the beam length  $a = b$  is applied in the calculations and the middle part of the structure is represented as the mass. For the analytical calculations there is no moment  $c_T$  applied. As there are two beams in the model the behavior of them can be written as,

$$X_1 = C_1 \cos\left(\lambda \frac{x_1}{a}\right) + C_2 \sin\left(\lambda \frac{x_1}{a}\right) + C_3 \cosh\left(\lambda \frac{x_1}{a}\right) + C_4 \sinh\left(\lambda \frac{x_1}{a}\right) \quad (1.23a)$$

$$X_2 = C_5 \cos\left(\lambda \frac{x_2}{a}\right) + C_6 \sin\left(\lambda \frac{x_2}{a}\right) + C_7 \cosh\left(\lambda \frac{x_2}{a}\right) + C_8 \sinh\left(\lambda \frac{x_2}{a}\right) \quad (1.23b)$$

With  $\lambda$  as

$$\lambda = \sqrt[4]{\frac{\rho A \omega^2}{EI}} a. \quad (1.24)$$

The eight boundary conditions with the mass interface from Fig. 1.5b,

$$w_1(0) = 0 \quad (1.25a)$$

$$M_b(0) = 0 \quad (1.25b)$$

$$w_1(a) = w_2(0) \quad (1.25c)$$

$$w'_1(a) = w'_2(0) \quad (1.25d)$$

$$M_{b1}(a) = M_{b2}(0) \quad (1.25e)$$

$$F_{Q1}(a) + m \ddot{w}(0) + F_{Q2}(0) = 0 \quad (1.25f)$$

$$w_2(l) = 0 \quad (1.25g)$$

$$w'_2(l) = 0 \quad (1.25h)$$

are implemented in the matrix from Eq. 1.26.

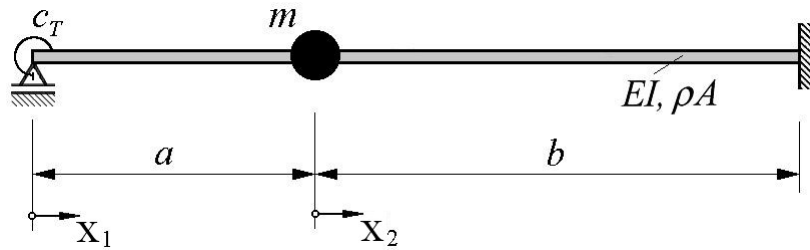
$$\begin{pmatrix} 1 & 0 & 1 & 0 & 0 & 0 & 0 & 0 \\ 0 & \lambda & 0 & \lambda & 0 & 0 & 0 & 0 \\ \cos(\lambda) & \sin(\lambda) & \cosh(\lambda) & \sinh(\lambda) & -1 & 0 & -1 & 0 \\ -\sin(\lambda) & \cos(\lambda) & \sinh(\lambda) & \cosh(\lambda) & 0 & -1 & 0 & -1 \\ -\cos(\lambda) & -\sin(\lambda) & \cosh(\lambda) & \sinh(\lambda) & 1 & 0 & -1 & 0 \\ \sin(\lambda) & -\cos(\lambda) & \sinh(\lambda) & \cosh(\lambda) & \frac{m\lambda}{\rho Aa} & 1 & \frac{m\lambda}{\rho Aa} & -1 \\ 0 & 0 & 0 & 0 & \cos(\lambda) & \sin(\lambda) & \cosh(\lambda) & \sinh(\lambda) \\ 0 & 0 & 0 & 0 & -\sin(\lambda) & \cos(\lambda) & \sinh(\lambda) & \cosh(\lambda) \end{pmatrix} \quad (1.26)$$

Now the linear system in Eq. 1.27 can be solved. With  $c$  as the vector with the unknown constants (like in Eq. 1.20). To get a solution the determinate (characteristic polynomial) must be zero Eq. 1.28. In the end an arbitrary number of eigenfrequency can be found with in Eq. 1.24. All this calculation could be done with MATLAB R2016b.

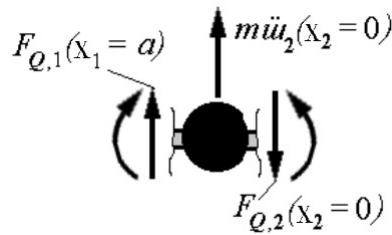
$$M \cdot c = 0 \quad (1.27)$$

$$f(\lambda) = \det(M) = 0 \quad (1.28)$$

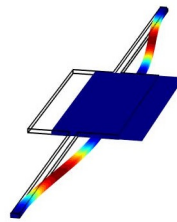
## 1 Basic Principle of Resonant Sensors



(a) The model for the analytical calculation. Source: Juergen Dankert [7]



(b) Mass in the middle of the model as interface between the beams. Source: Juergen Dankert [7]



(c) The initial structure used for the simulations in COMSOL, short side view.



(d) The initial structure, long side view.

**Figure 1.5:** Comparison of the model for the analytical calculation and for the FEM simulation. The middle part is represented as the mass. The beams are fixed on both sides, later one side will be displaced out of the plane.

It is also possible to use the Ritz method or finite difference method in MATLAB, but the only other used calculation method was FEM. In Fig. 1.6 one can see a comparison between the analytical model, calculated with MATLAB and the FEM simulation of the structure in COMSOL (Fig. 1.5c and Fig. 1.5d). These are the eigenfrequency values for the first out-of-plane mode for four different beam lengths. It is important to note

that the beam length is not the length of the whole structure, as there is a middle part as well. The whole structure length is, therefore, two times the beam length plus the middle part length. With doubling of the beam length the frequency should decrease by a factor of 4 ( $\Omega = 1/L^2$ ), for a simple beam. This is approximately the case in Fig. 1.6 up to a beam length of 150  $\mu\text{m}$ . Above this value the interference of the middle part with its additional mass changes this characteristic, the exponent  $L^n$  gets smaller than  $n = 2$ . The comparison between the analytical calculation and FEM simulation are very satisfying since the values deviate less than seven percent. The exact simulation setup will be discussed in Ch. 2.1.

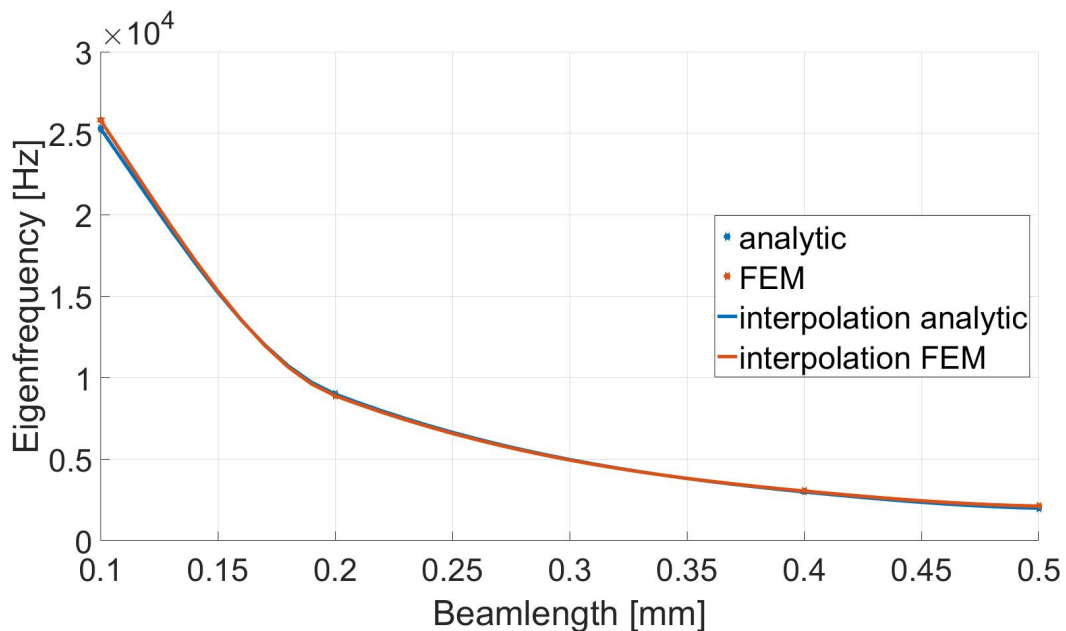


**Figure 1.6:** Comparison of the analytical calculation and the FEM simulation. The beam length varies on four values 100  $\mu\text{m}$ , 200  $\mu\text{m}$ , 400  $\mu\text{m}$  and 500  $\mu\text{m}$ . The deviation is less than seven percent on each point. The eigenfrequency is proportional to  $1/L^2$ , this is visible below 150  $\mu\text{m}$ . The deviations above are caused by mass of the middle part of the structure. This part has a fixed length and mass, therefore, the change of the beam length changes the eigenfrequency partially only.

### 1.4 Lumped-Element Model Resonator

Another method to simplify an oscillating system is the lumped-element model. Parameters like the Q factor can be estimated with a simple energy model, this model takes in account that the system always dissipate energy through damping, but does not distinguish between different mechanism and their frequency dependence. If an oscillating system is driven in a linear regime, the system can be modeled by lumped elements see Fig. 1.7. Here, the behavior of a point on the resonator can be written as second order differential equation

$$m\ddot{z} + c\dot{z} + kz = F(t), \quad (1.29)$$

where  $m$  is the total mass,  $k = F/l$  is the spring constant, and  $c$  is the damping coefficient. A special case would be the free undamped vibration, as the name implies there is no damping  $c = 0$  and  $F(t) = 0$ . As the kinetic and potential energy must be equal, one can write

$$\frac{1}{2}m\dot{z}^2 = \frac{1}{2}kz^2 \quad (1.30)$$

yields the eigenfrequency, with Eq. 1.29,

$$\Omega = \sqrt{\frac{k}{m}} \quad (1.31)$$

This will be important in 2.2.2, when the actions for improving of the sensor structure will be deliberated.

### 1.5 Summarized Fabrication Process

For the measurement and comparison of the new designed sensor an already existing sensor was used. The following should give a short overview how this sensor was fabricated. The particular mounting of the sensor for this thesis is described in Ch. 5.1.1.

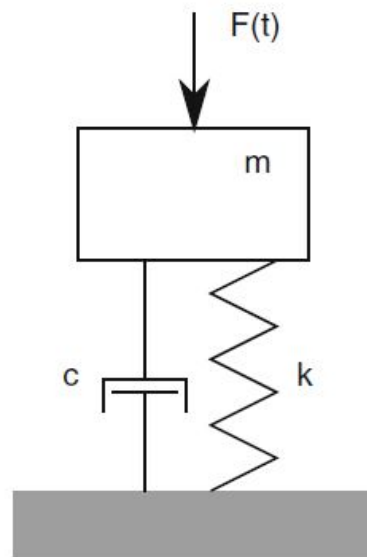


Figure 1.7: Lumped-element model resonator, to describe the resonant behavior of the beam [13].

The sensor is fabricated on a 100 mm SOI-wafer with  $\langle 100 \rangle$  orientation. The handle wafer is 350  $\mu\text{m}$  thick, the buried oxide layer 250 nm and the Si-device layer 20  $\mu\text{m}$ . The fabrication process flow is in Fig. 1.8: Step I and II show the structuring of the Pt layer with a lift-off technology. A gold layer is created with the same procedure in step III and IV. In V and VI an etching mask is structured for the following dry etch process in step VII. Afterwards the surface is protected with a resist and etched from the other side like in step V and VI. Now the sensor is only connected with the suspension structure [4]. Afterwards the sensor was connected with Au-bonding to a PCB-board for an easier handling, the finished sensor is pictured in Fig. 5.3.

## 1 Basic Principle of Resonant Sensors

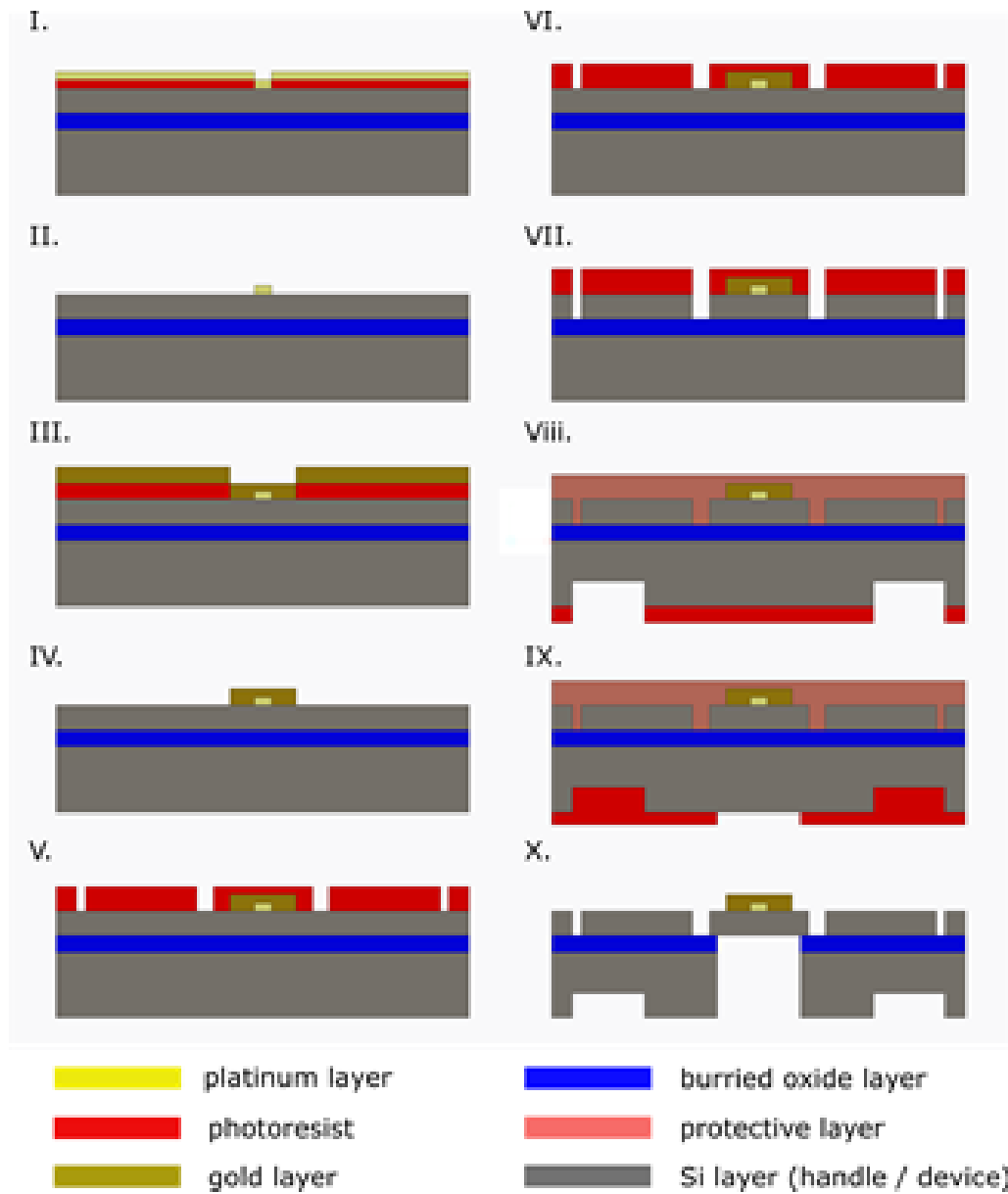


Figure 1.8: Fabrication process of the sensor using deep reactive ion etching and lift of technique. The middle part with the gold layer is the sensor structure [4].

## 2 Simulations

This chapter describes, first, the simulation setup for the mechanical FE-Model and, second, the development of the final design, with all ideas and parameter variations, finally an already existing sensor is simulated and compared to the new design which is in some aspects too optimistic. Some of the structure features are too ambitious for the current technological processes at the Institute, at least wafer level. Anyway, this reveals the ways to future designs to achieve. The simulation compared to the measurements results are also important to confirm the new design in Ch. 5. All these simulations were done with the FEM software COMSOL V5.2. These kind of simulations are generally important for the development of MEMS, since a trial and error working process would be too expensive and too time consuming, due to the large turn around time for a new MEMS device.

### 2.1 Simulation Setup

To find an appropriate sensor structure many different designs and parameters have been investigated. The corresponding procedures are described in this chapter. Initially, an analytical model of a simplified structure was calculated (see Ch. 1). This should give an overview and an idea where the resonance frequency will be and how the different parameters influence the characteristic of the structure. To have a more realistic simulation one external damping factor, air damping was included, that was considered by boundary loads on every surface. The load accords to sea level standard

## 2 Simulations

atmospheric pressure (1013 hPa). The "solid mechanics" interface was mainly applied for the simulations. In COMSOL the calculation part starts with the "study setup", where a parameter sweep can be configured that allows the variation of the values for the structure geometries and of course the displacement. The next step is the so called "stationary", where the deformation, stress and strain in the equilibrium state are calculated. This is followed by "eigenfrequency", that is only needed if the resonance frequency should be calculated. Usually, only the in-plane mode is interesting for this thesis, but the desired mode is not always the first one to be found. Sometimes torsional and out-of-plane modes are found before. The out-of-plane mode is interesting in relation to the analytic model and the validation of the measured data. An appropriate mesh has to be created since a wider mesh saves simulation time but causes larger errors. Due to the high aspect ratio of the beams, they are thin and long, about 150000 domain elements are required.

### 2.2 Model Implementation and Development

For the simulation of the static displacement, the beam or beams are fixed on one side and cannot move in any direction. On the other side the beams can only move in the out-of-plane direction Fig. 2.1. The in-plane and parallel direction are fixed as well. This should emulate the bending of the beam. The initial model is depicted in Fig. 1.5c, the relevant geometrical parameters values are listed in Tab. 2.1. Unless otherwise stated, the simulated model uses the parameters as listed in the table.

Parameter	Value
Material	isotropic Si
Beam length ( $\mu\text{m}$ )	100
Beam width ( $\mu\text{m}$ )	2
structure height ( $\mu\text{m}$ )	5
middle width ( $\mu\text{m}$ )	75
middle length ( $\mu\text{m}$ )	50
hole width ( $\mu\text{m}$ )	0
hole length ( $\mu\text{m}$ )	0

Table 2.1: Initial model values in COMSOL

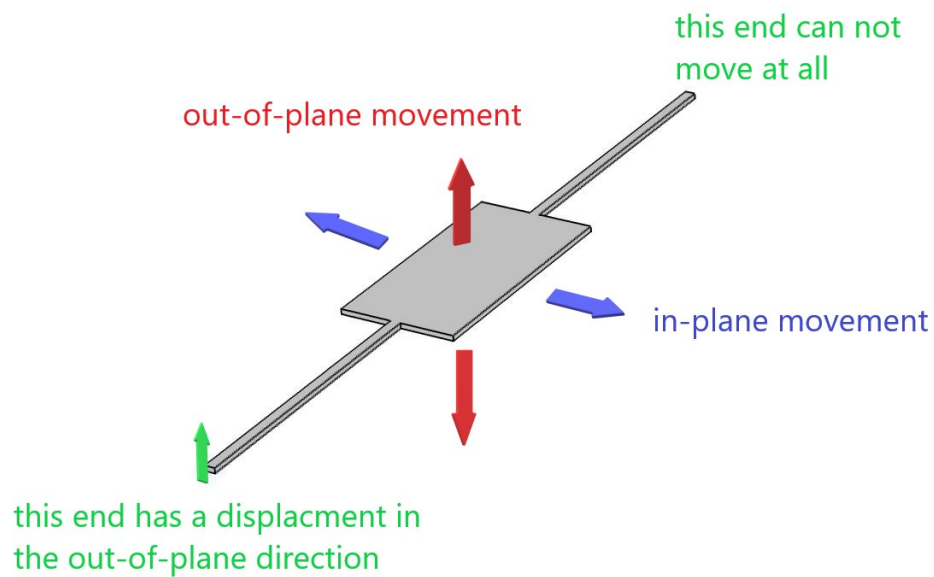


Figure 2.1: Simulation model with boundary conditions for the displacement and directions for the investigation of the mode shapes.

## 2 Simulations

### 2.2.1 Initial Point

The first idea of the sensor was a simple double clamped beam with a wider area in the middle of the beam, as pictured in Fig. 1.5c. The middle of the beam should give more flexural rigidity for the in-plane mode and the possibility for an actuation with a piezoelectric crystal resonator. However, the initial structure did not have a sensitivity for displacement in the sub-nanometer region, therefore, an analysis of the parameter influence on the structure was necessary.

### 2.2.2 Parameter Variation

To have an idea which parameter should be changed to improve the responsivity of the sensor structure, one can look at the AFM which works in a similar way. The AFM has a frequency response  $\mathfrak{R}$  caused by a force  $F$ , as in Eq. 2.1 (for the functionality of the AFM see [11]). This force causes a bending of the beam in the  $z$  direction. As calculated in [13] chapter 3.2.2 and explained in the following, one can see that the relative response is proportional to the spring constant  $k$  (Eq. 2.3). It can be implied that a low spring constant, also called soft resonator, results in a higher responsivity. There are three different ways for increasing the responsivity, as described in [14], smaller dimensions, usage of a material with smaller Young's modulus and introduction of stress concentration regions (SCR). In case of this sensor it is almost the same, only that bending of the structure is directly induced with the displacement on the edge of the structure.

$$\Delta F = \mathfrak{R}^{-1} \Delta z . \quad (2.1)$$

If a resonator vibrates with the amplitude  $z$  around its equilibrium position  $z_0$  the measured force can be approximated by a Taylor series

$$F(z_0 + z) \approx F(z_0) + \frac{\partial F(z_0)}{\partial z} z , \quad (2.2)$$

if the derivative of the force is not zero,

$$\frac{\partial F(z_0)}{\partial z} = F'(z_0) \quad (2.3)$$

the lumped-element equation from Eq. 1.29 can be written as

$$m\ddot{z} + c\dot{z} + kz = F(z_0) + F'(z_0)z \quad (2.4a)$$

$$m\ddot{z} + c\dot{z} + (k - F'(z_0))z = F(z_0) \quad (2.4b)$$

$F(z_0)$  pushes the resonator into a new equilibrium point, but can be assumed as a small force and be negligible for a linear system. With Eq. 1.31 for the eigenfrequency turning to

$$\Omega = \sqrt{\frac{k - F'(z_0)}{m}} = \Omega_0 \sqrt{1 - \frac{F'(z_0)}{k}} \quad (2.5)$$

if the term with the derivative of the force is assumed to be small compared to 1,  $\Omega$  can be approximately describes as

$$\Omega \approx \Omega_0 \left( 1 - \frac{F'(z_0)}{2k} \right) \quad (2.6)$$

With these equation the frequency responsivity  $\Re$  and the relative frequency responsivity  $\partial\Re$  can be calculated as

$$\Re = -\frac{\Omega_0}{2k} \quad (2.7a)$$

$$\partial\Re = -\frac{1}{2k} \cdot \quad (2.7b)$$

### 2.2.2.1 Graph Description for the Parameter Variation

For each parameter variation a graph with the simulation results was created. For the sake of clarity only the most relevant results are included in the respective graphs. Since the eigenfrequency varies very strongly with the parameter variation, the graphs also show the relative change of the eigenfrequency like in Eq. 2.8, if not otherwise

## 2 Simulations

specified. The increment size of the displacement,  $x_{i+1} - x_i = 100$  pm, is unchanged for these simulations, as the relative eigenfrequency depends on it. The responsivity slope is usually only simulated for a small range in a linear area, since the simulations would take a very long time if they were taken over a longer period with a small resolution.

$$\Omega_{relative} = \frac{\Omega(x_{i+1}) - \Omega(x_i)}{\Omega(x_0)} \quad (2.8)$$

### 2.2.2.2 Variation of the Beam Length

As shown by Eq. 2.7b a low spring constant should be desirable. This can easily be achieved by increasing the beam length. However, there is a major drawback, because by doubling the beam length the resonance frequency will decrease with a factor of four, as shown in Eq. 1.22. Fig. 2.2 depicts the relative change of the resonance frequency caused by the displacement of the structure. The largest beam has also the highest change in resonance frequency, but unfortunately a frequency of 2000 Hz for the 1000  $\mu\text{m}$  beams is very low, while at 50  $\mu\text{m}$  the resonance frequency is at 170 kHz. This is described in the study of Shengli Kong [15]. There the relative eigenfrequency saturates with increasing beam length and constant beam width. What is interesting as well is the other direction in Fig. 2.3, because here the relative eigenfrequency is going to infinity, a ratio of 0.1 should not be undercut. The simulation indicates this behavior as with a larger beam length the simulation setup gets to its limits, as one can see with the increasing of variations caused by simulation errors in  $\Delta\Omega$  (Fig. 2.2). To get better results the simulation mesh must be finer, which would drastically increase the simulation time, but this is unnecessary as this results already show that a beam length under 150  $\mu\text{m}$  would be an improvement of the initial structure.

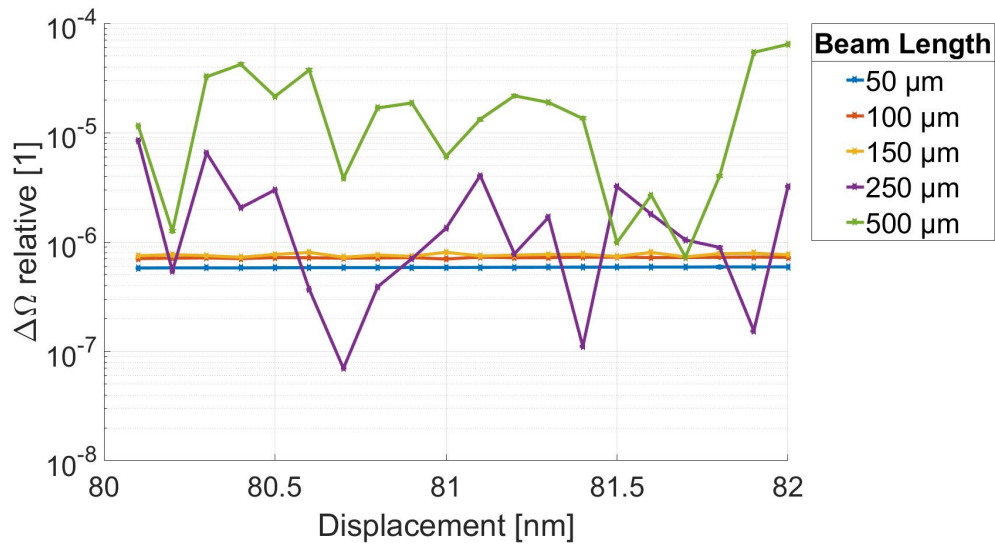


Figure 2.2: Variation of the beam length and the relative change of the resonance frequency in the displacement range: 80 nm - 82 nm. Beyond a beam length of 150  $\mu\text{m}$  the variations caused by simulation errors get higher. Probably because the ratio between length and width gets less than 0.1, what is not ideal for the simulation setup.

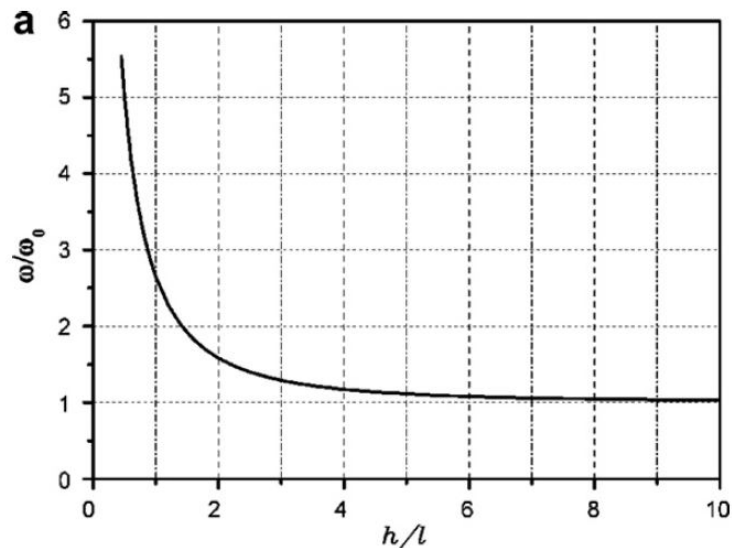


Figure 2.3: Dependence of the relative changes of the eigenfrequency on the height to length ratio [15]. The ratio, height to length, is here depicted although the ratio width to length is more relevant for the presented sensor design.

## 2 Simulations

### 2.2.2.3 Variation of the Beam Width

It is stated in [15] that in order to get a relatively high resonance frequency the ratio between height and length  $h/L$  must be high. Since the in-plane mode is investigated with highest priority in this thesis, width and height switch place. Now width and length must fulfill this ratio. Here, the same ratio must be minded as in 2.2.2.2, with the difference that the enumerator of the ratio is observed now.

The resonance frequency depends strongly on the width. At a width of 10  $\mu\text{m}$  the frequency is with 50 kHz very high, but the responsivity is around 0.1 Hz/nm. Fig. 2.4 illustrates that the responsivity changes continuously with the beam width. For a beam width less than 0.3  $\mu\text{m}$  the simulation exhibits large variations caused by simulation errors as in 2.2.2.2, when the ratio is below 0.1. Therefore, the beam width 0.3  $\mu\text{m}$  was chosen for the final design. One has to consider that this small structure size could not be fabricated on the institute, but it still shows the potential of the principle and the possible responsivity values.

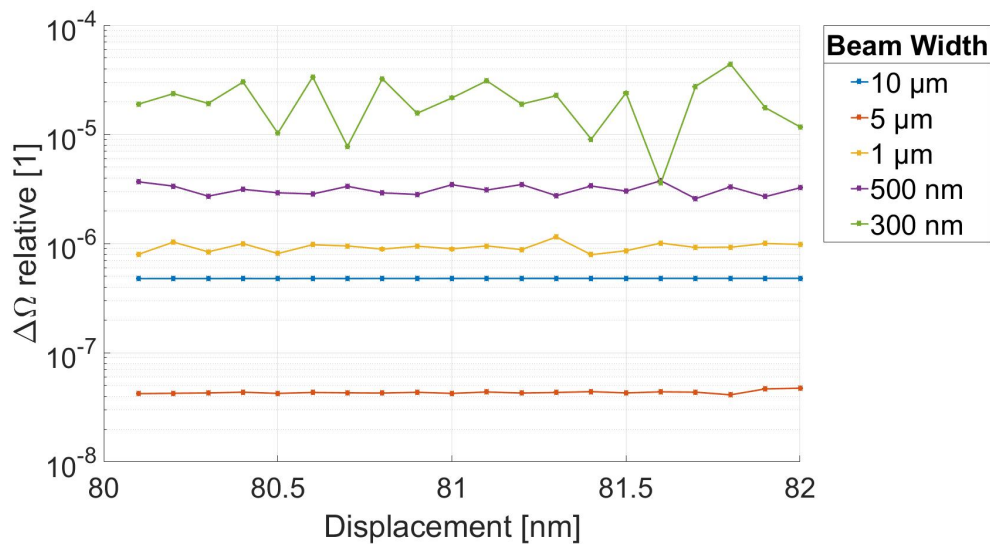


Figure 2.4: Variation of the beam width and the relative change of the resonance frequency with displacement (displacement range: 80 nm - 82 nm). The variations caused by simulation errors start to increase beyond a beam width of 300 nm, like at the simulation with the beam length.

### 2.2.2.4 Multiple Beam Design

The use of multiple beams can increase the sensitivity in different ways, like utilizing DETF (Double-Ending Tuning Fork) that uses two beams to measure small forces in the axial direction, as shown by Gui and Li [5]. The simulations in this thesis revealed that displacement in the out-of-plane direction at the multiple beam structure can not be measured as good as in the axial direction, since a displacement in the axial direction causes much higher stress than in out-of-plane direction. However, the number of beams beneficial influences useful effects, as described below. One problem with long beams is the decrease of the resonance frequency, as shown in Fig. 2.2. A large number of beams can reduce this problem, since the resonance frequency increases again without reducing the responsivity. This behavior is displayed in Fig. 2.6, which shows that the relative sensitivity is constant through out all variation and that the absolute sensitivity rises, except for one beam. Despite nonlinearity increases strongly after the amount of five beams. The benefit is depicted in Fig. 2.6b, here one can see clearly that the resonance frequency increases according to the number of beams in the structure. The design grows about two beams on one side for each step (one, three, five and seven beams) and can be viewed in Fig. 1.5c and Fig. 2.5. The position of the previous existing beams is always the same.

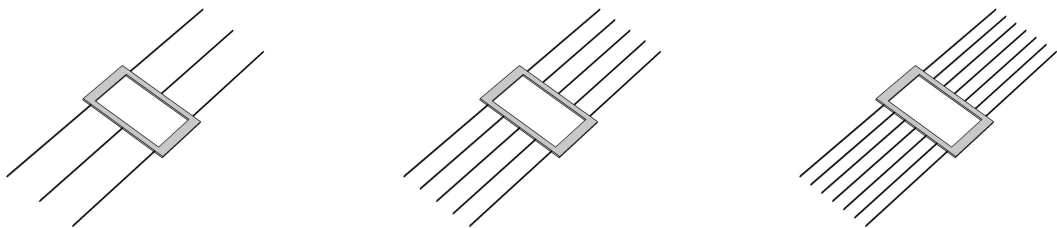


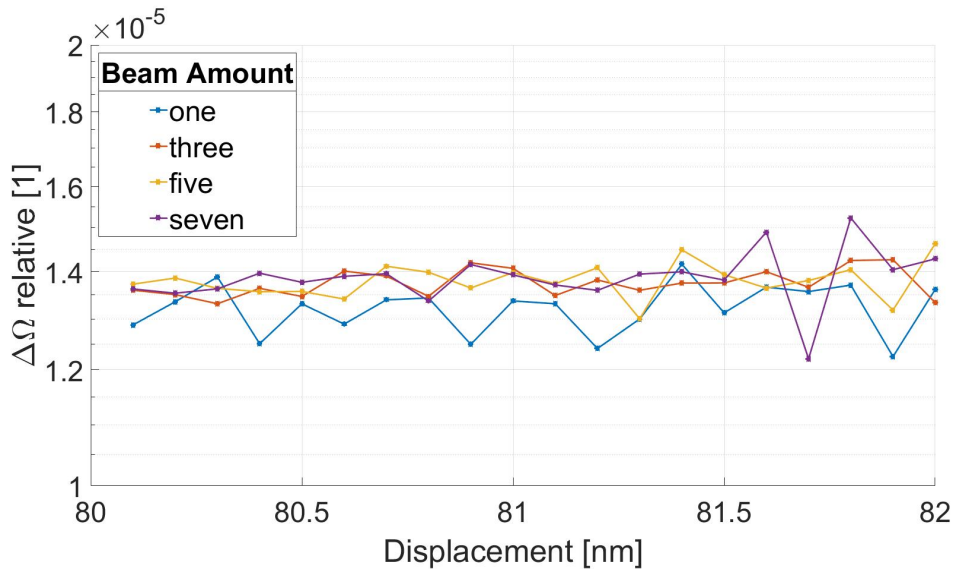
Figure 2.5: Development of the multiple beam design, with three, five and seven beams on one side.

## 2 Simulations

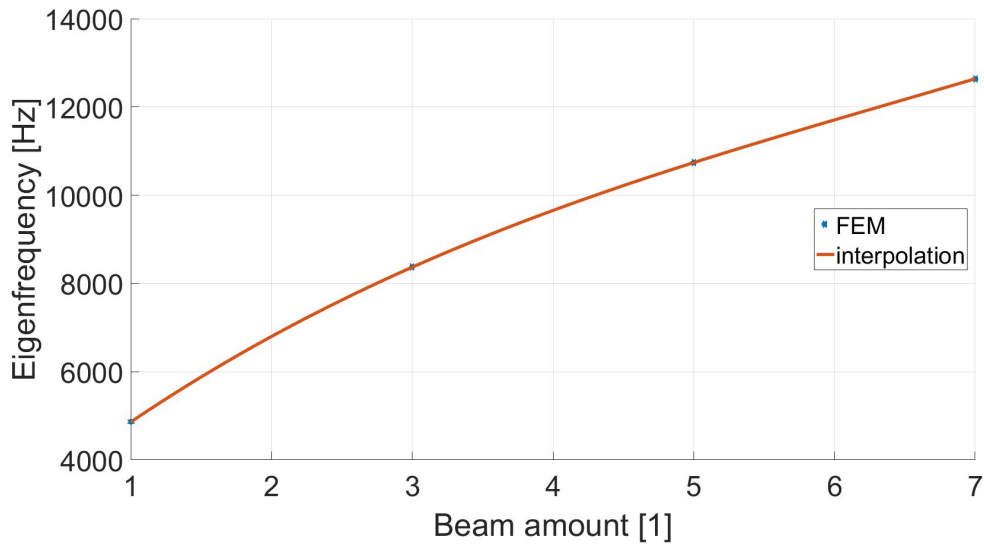
The cause of this effect and the step from one to three beams can be the introduction of stress concentration regions (SCR). Usually these regions are just small holes in a cantilever, but the multiple beam structure can also be viewed as one beam with holes in it. These holes, as it is described in Sh Mohd Firdaus and Azid [14], increase the stress in the beam. This stress has an impact on the eigenfrequency, therefore, on the sensitivity. The step from one to three beams on one side is the relative largest and hence causes the biggest change. As described in [14] increasing the number of holes, does not increase the stress in the same way, meaning that a low number of holes is sufficient. This effect can be easily implemented, as it requires only additional structures that are formed (etched) with the same process as the beams, needing no additional mask and technological processes.

A similar effect can be seen in Fig. 2.13, where the beam is in the regime with very low displacement not very sensitive, this increases with higher displacement and therefore with more stress in the beam. One can conclude that the sensor should work with some pre stress. The increase of the eigenfrequency can be mathematically expressed by with an extension of Eq. 1.22. As described in [13] a beam under stress can be separated into an unstressed beam and a term with tensile stress  $\sigma$

$$\Omega = \sqrt{\frac{Eh^2n^4\pi^4}{12\rho L^4} + \sigma}. \quad (2.9)$$



(a) Variation of the beam amount on one side of the structure and the relative change of the resonance frequency with displacement. Displacement range: 80 nm - 82 nm



(b) Increase of the resonance frequency corresponding to the amount of beams on one side of the structure, without displacement.

Figure 2.6: COMSOL simulation of the beam amount without any displacement.

## 2 Simulations

### 2.2.2.5 Variation of the Structure Thickness

The height has in this case barely any influence on the resonance frequency and even less to the sensitivity, as Eq. 1.22 shows. Only when the thickness is lower than  $1.5\ \mu\text{m}$  a variations caused by errors through the simulation occur (Fig. 2.7). Note, again one has to switch the influence of width and height since the in-plane mode is observed.

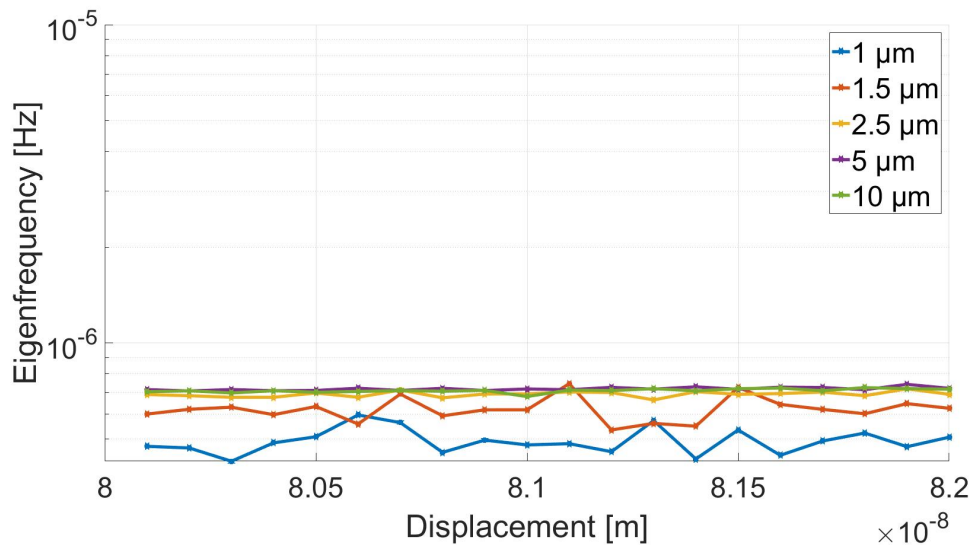


Figure 2.7: Influence of the beam thickness and displacement on the relative change of the resonance frequency (Displacement range: 80 nm - 82 nm).

### 2.2.2.6 Mass Reduction with Hole

The impact of the mass can be seen in the analytical model. It reveals that with a reduction of the mass one should expect a higher resonance frequency. One possibility would be the use of a material with lower density. However, this is often accompanied with a smaller Young's modulus which reduces the resonant frequency. With the available MEMS technology silicon as material for the vibrating structure is, therefore, a perfect choice. Another possibility to reduce the mass of the structure is the introduction of a hole in the middle part. Figure 2.8 shows the impact of the weight in the center

region of the structure. The larger the hole is the higher the resonance frequency will be. This effect is confirmed by the analytical model (see Fig. 1.5a) and the FEM simulation. While the characteristic of the analytic calculation is parabolic, the FEM simulation has an interesting form, when the size of the hole is very small the eigenfrequency increases faster, but is almost constant at a hole size of  $500 \mu\text{m}^2$  to  $750 \mu\text{m}^2$ . Probably the mesh size was too coarse for the small hole dimension at the area lower  $200 \mu\text{m}^2$ .

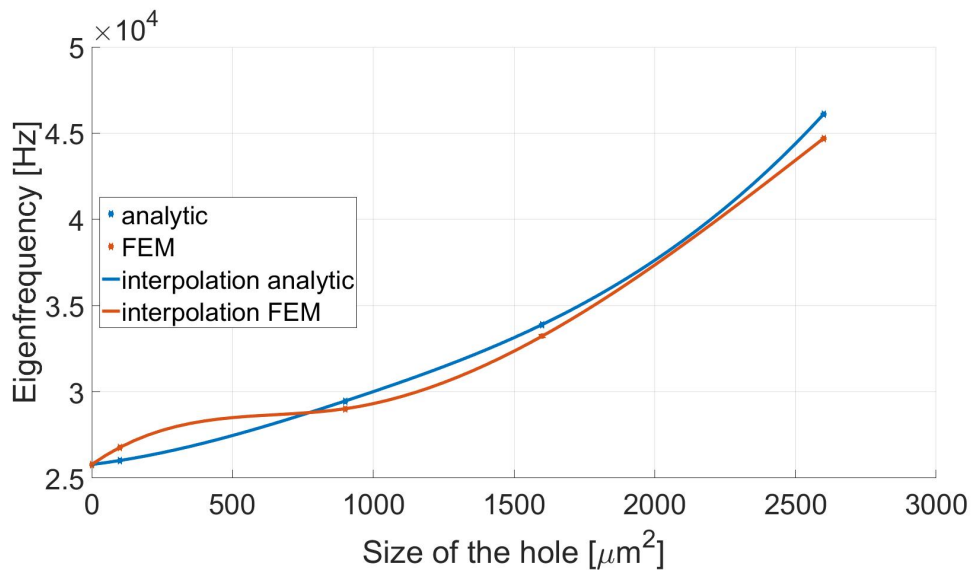


Figure 2.8: Influence of the hole in the structure with resulting increase of resonance frequency.

### 2.2.2.7 Variation of the Material

Equation 1.22 demonstrates how the resonance frequency depends on material attributes, like the Young's modulus and the density. Consequently, different materials should be considered, as the Young's modulus varies strong for different materials, as shown in Fig. 2.9.

## 2 Simulations

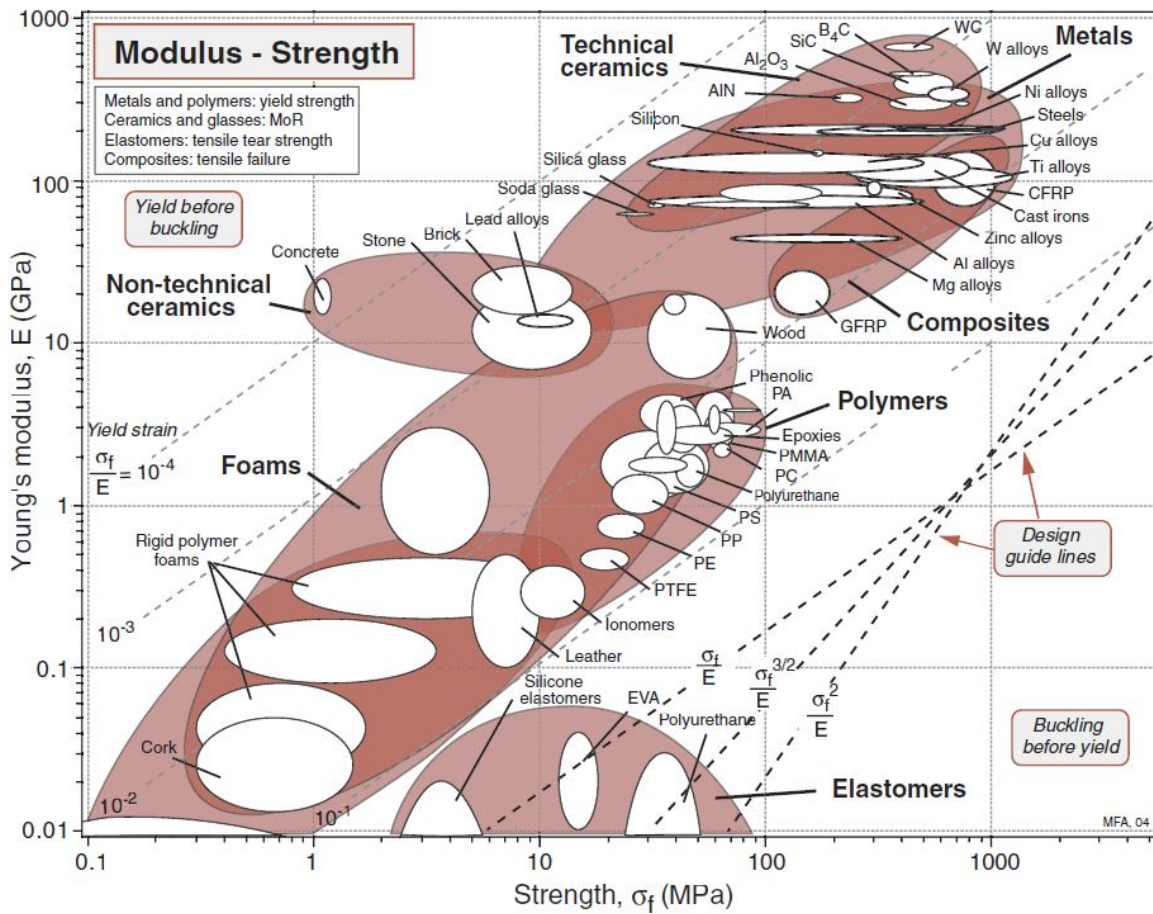


Figure 2.9: Materials Selection in mechanical design, Michael F.Ashby (chapter 4.3).

In order to show the impact of the material the same structure was simulated with three different materials. The former standard material silicon, silicon carbide in the 6H phase and silicon oxide. The most important material values are found in Tab. 2.2. One should expect a high resonance frequency for SiC caused by the large ratio  $E/\rho$  but a low relative responsivity. The simulations show something unexpected, namely SiC having much better results than Si and  $SiO_2$ . SiC has with 120 kHz a much higher resonance frequency but the responsivity is also much higher, although it is not a soft resonator as desired. As already stated in Ch. 2.2, this is due to the fixed displacement. Therefore, the force (with  $F = k \cdot l$ ) or stress for the deflection has to be much higher in SiC than in Si in order to get the same displacement. This effect can still be interesting

Material	Young's modulus (GPa)	Density (kg/m <sup>3</sup> )	$E/\rho$ (kPa kg/m <sup>3</sup> )
Isotropic Silicon Si	170	2329	73
Silcon Carbid SiC(6H)	748	3216	233
Silicium Oxide SiO <sub>2</sub>	70	2200	32

Table 2.2: Material attributes from COMSOL, the values are slightly higher then in Fig. 2.9 as these are values for mono crystals.

if the structure is implemented into a much larger environment and therefore the force is negligible. Unfortunately, different materials also require the application of different processes during the fabrication, for example during etching.

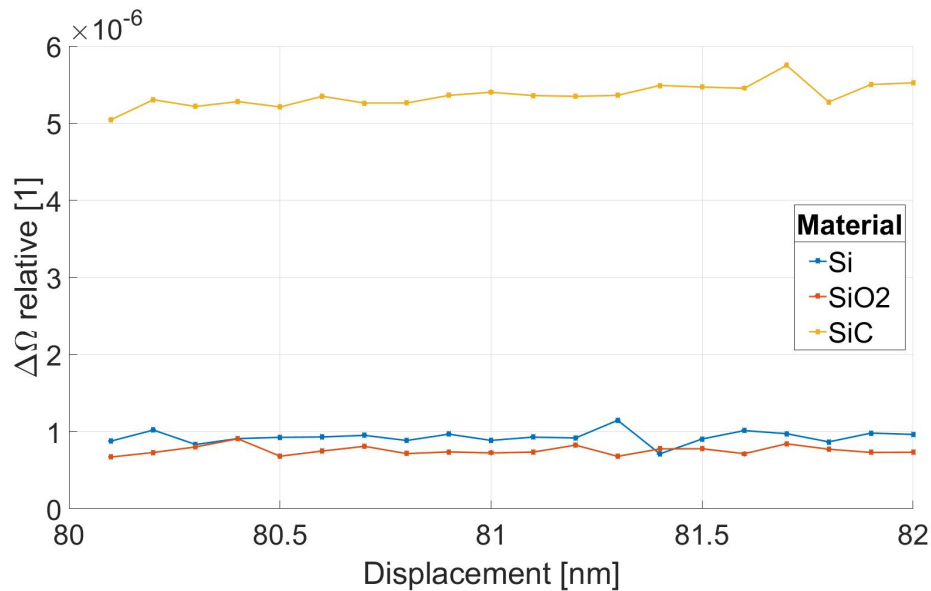


Figure 2.10: Variation of the material and the relative change of the resonance frequency with displacement. (Displacement range: 80 nm - 82 nm).

## 2.3 Final Design

All of the parameter variations were combined and simulated. After many trial runs, the design pictured in Fig. 2.11 finally showed the best results. Geometric and material parameters from the structure are listed in Tab. 2.3. The change of the resonance frequency with displacement is depicted logarithmic in Fig. 2.13. At small deflection the slope of the curve reaches zero and so the responsivity. At a displacement of 100 nm the responsivity is 2 Hz/nm and increases at 200 nm to 3.4 Hz/nm. The slope of the sensor would clearly fulfill the goal of this thesis, but not all damping factors are considered. Here, the packaging and also required leads on the structure have to be mentioned. In Fig. 2.12 one can see the excursion of the structure in the first in-plane mode with an amplitude of about 80 nm.

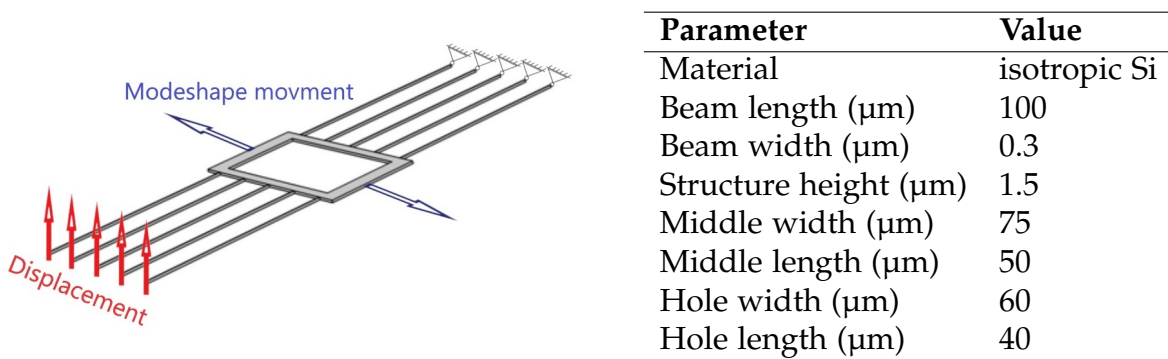


Figure 2.11: Final design in COMSOL. One side is clamped, the other side will be displaced. The mode shape movement follows the blue arrows.

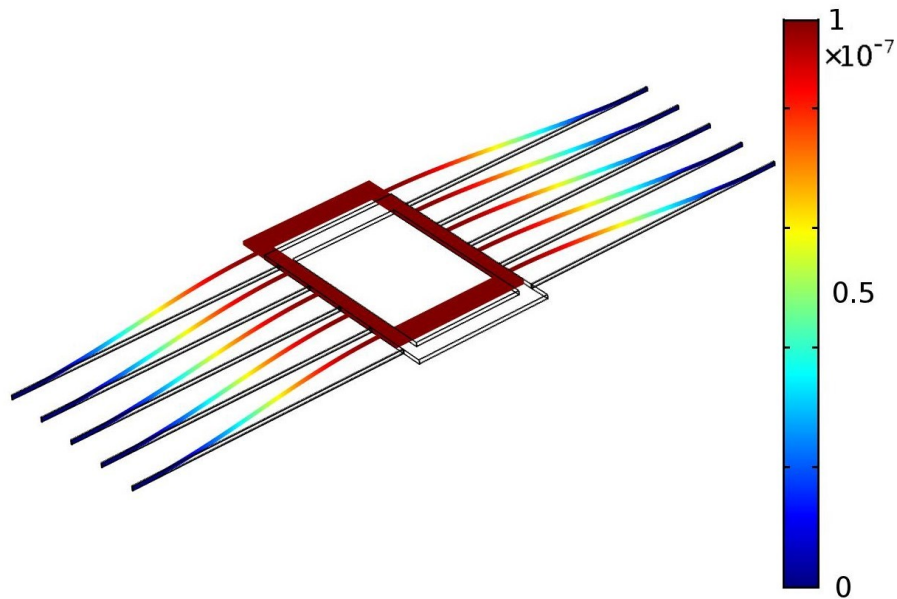


Figure 2.12: Final design of the sensor depicted with the first in-plane vibration, exported from COMSOL. The color indicates the vibration amplitude in nanometer, as the beams are fixed at the ends the maximum occurs in the middle.

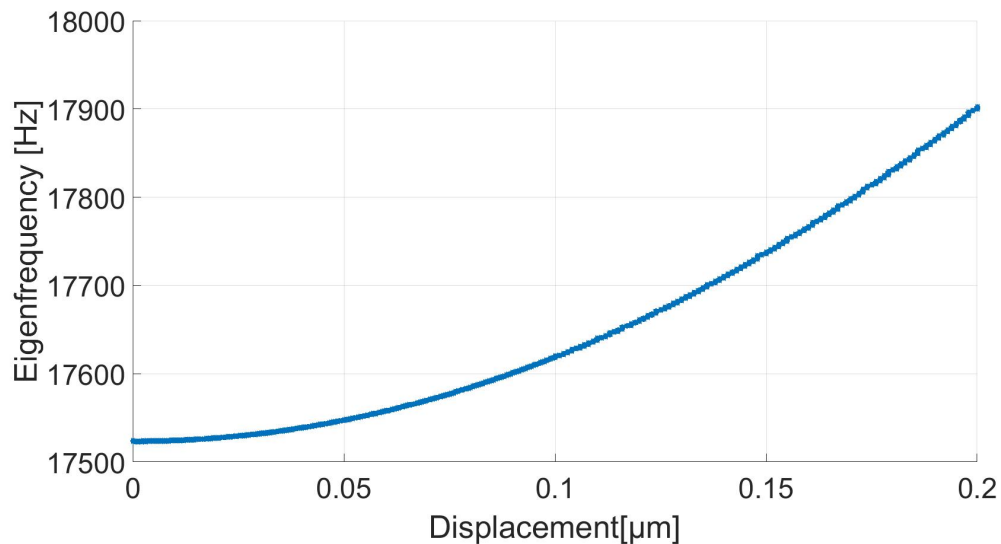


Figure 2.13: The eigenfrequency of the final design. Without any displacement the structure is not sensitive at all, but with increasing displacement the eigenfrequency increases nonlinear. Although one could expect a form like  $\sqrt{\sigma}$ , this effect can only be observed in the measurement. This deviation could be caused by the difference between displacement the fixed displacement in COMSOL and the bending in the measurement.

## 2 Simulations

### 2.3.1 Fabricated Sensor

For verification of the simulation, an existing design (as illustrated in Fig. 2.16) was used for the measurement and tested under the planned conditions. This sensor type has a different design and dimensions than the previously described structures. Therefore, it is not straight forward to compare them. The sensing structure is designed like a cross, which enables to measure five mechanical degrees of freedom (two force and three torque components) as depicted in Fig. 2.14. The sensing structure is connected via a sub-structure to a frame. This sub-structure should compensate the influence of temperature, as there occurs a temperature difference between the small thin sensing structure and the thick frame which results to stress and therefore a detuning of the resonance frequency. As the protecting frame is due to its thickness much stiffer, a meander was integrated to be able to bend the whole sensor structure. For this thesis only the simulation setup as described in Ch. 2.1 was interesting. As the dimension of the beam length of the sensing structure is about 2.85 mm the width 0.13 mm and the height 0.5 mm a mesh number with about 200000 degree of freedom was used. The responsivity is not as high as that of the described in Ch. 2.3. This is caused by the different dimensions (length and width or height, dependent on the eigenmode shape off the structure). When this sensor is simulated with the same displacement principle as the one designed for this thesis, the third mode (out-of-plane) exhibits the highest responsivity of 2 Hz per 100 nm, which is about a factor of 165 lower then the responsivity of the new designed. This indicates the huge potential for further improvements. The fabricated sensor is a suitable principle, which is described in detail in Ch. 5 is not as important as the comparison should only view that improvement is possible.

A FE-model of the structure of the fabricated sensor was created in COMSOL. The corresponding results of the dependence of the responsivity in the displacement are depicted in Fig. 2.15. The curve has the same shape as in Fig. 2.13, which is due to the fixed displacement during the simulation.

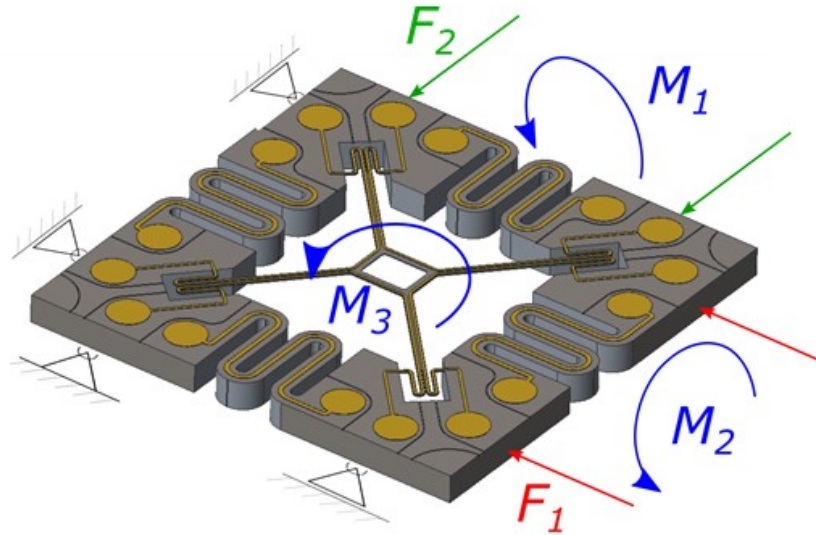


Figure 2.14: Fabricated design, with all intended five mechanical degrees of freedom [3].

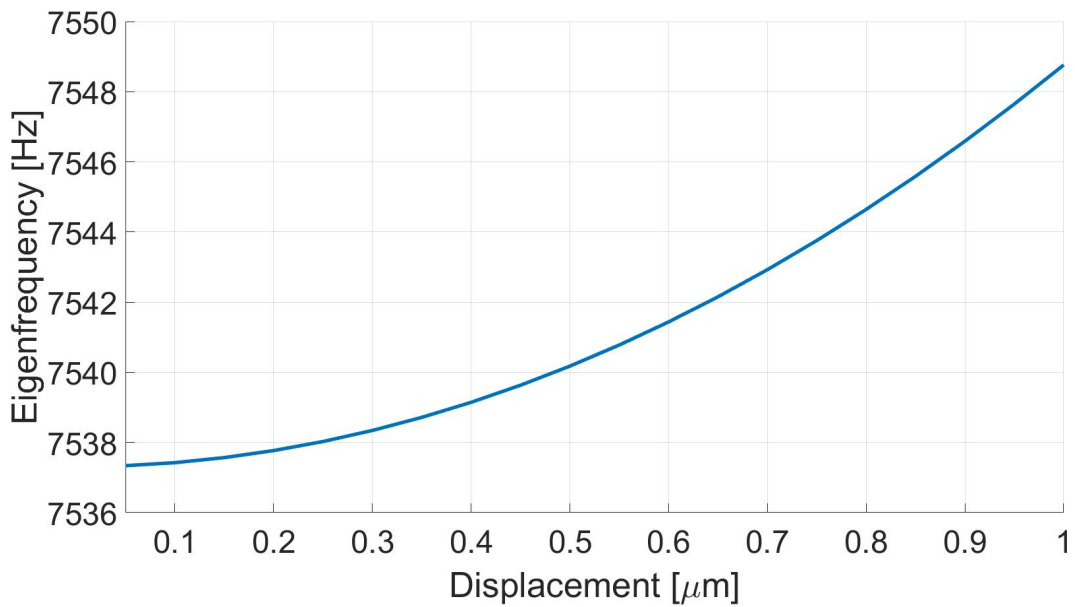


Figure 2.15: Simulation of the alternative sensor to validate the newly designed sensor. The eigenfrequency increases with the displacement and therefore with the tensile stress  $\sigma$ , like it is shown in Eq. 2.9. The responsivity is about 2 Hz per 100 nm.

## 2 Simulations

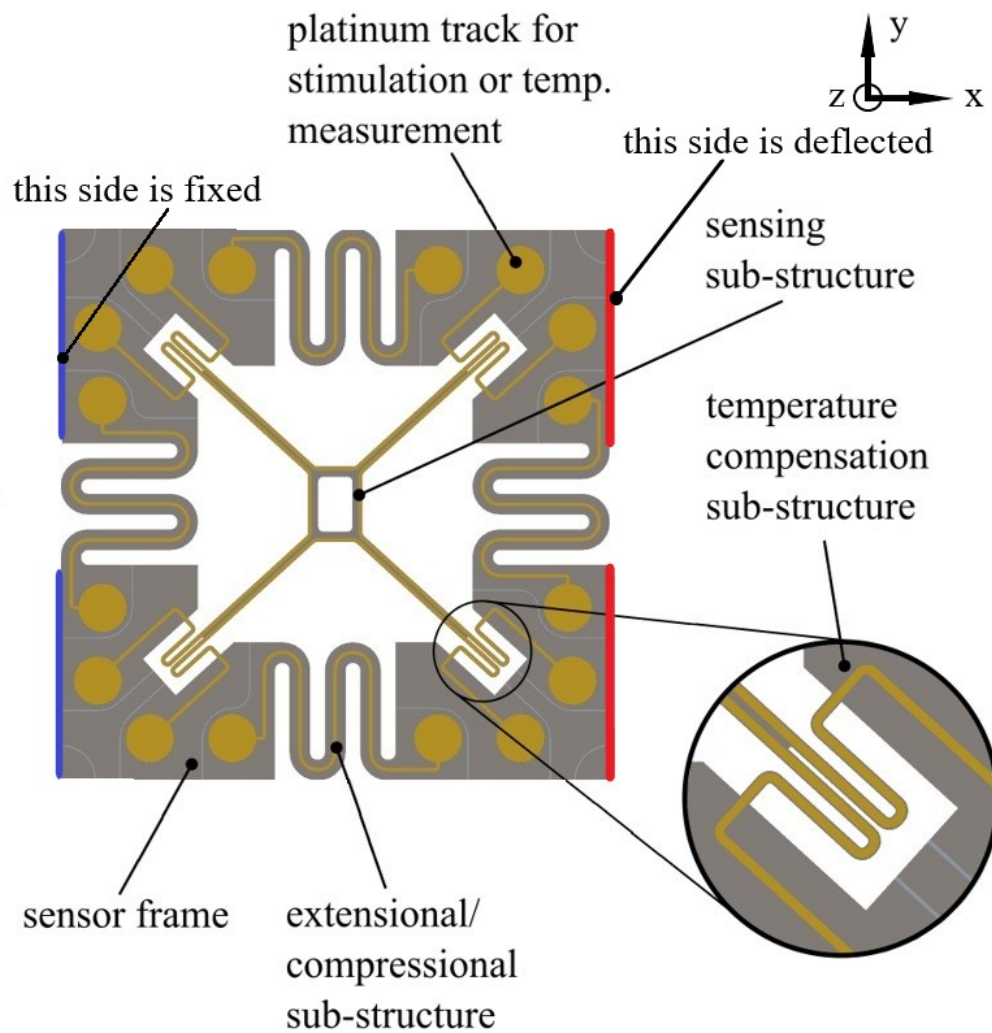


Figure 2.16: The suspension on the sensor frame reduces the stiffness and enables an easier bending of the structure. The golden points and lines are platinum leads for the Lorentz force actuation [3].

## 3 Readout

In order to measure the change of resonance frequency, one has to measure the frequency of the vibration. First, the beam or structure has to be excited (Ch. 4) and the amplitude of the vibration of the beams has to be read out. The excitation can be done, e.g. by Lorentz force actuators or electro-statically. The optical readout method is a very convenient principle to be implemented, especially during sensor development. When the MEMS structure is not packaged and, therefore, fully accessible. Consequently, this method was applied in this stage of sensor development.

The inductive readout requires an external magnetic field (e.g. permanent magnet) and is not that sensitive like the optical one, but a candidate for being integrated on the MEMS-chip. The capacitive readout exploits changing capacities due to the vibration of the beam, it requires electrodes on the beam and fixed ones which are more difficult to be implemented since small gaps are required for high sensitivities. The piezoelectric readout requires the deposition (and polarization) of piezoelectric materials. These materials are currently difficult to process on MEMS devices and are, therefore, not so favorable. This technology would have a major advantage, because it is possible to use the same layer for sensing and actuation. A very common way is the piezo-resistive readout, which is usually made with doped regions on the SI-wafer and a Wheatstone bridge. This technology would have a major advantage, because it is possible to use the same layer for sensing and actuation.

### 3.1 Piezo-resistive Readout

Here the piezo-resistive effect (PRE) is utilized. It describes how the electrical resistance changes due to mechanical stress, compressional or tensile. Since the aim is to measure the change in the resonance frequency the magnitude of the piezo-resistive effect is not that important.

The base of the PRE is the very common Eq. 3.1 with the material specific resistance  $\rho$ , the length of the conductor  $l$  and the area  $A$ ,

$$R = \rho \frac{l}{A}. \quad (3.1)$$

The resistive change  $\Delta R$  is the sum of the changes of each factor [13]

$$\Delta R = \Delta \rho \frac{\partial R}{\partial \rho} + \Delta l \frac{\partial R}{\partial l} + \Delta A \frac{\partial R}{\partial A}. \quad (3.2)$$

The first factor represents the changing resistivity due to mechanical stress. Especially in semiconductors the stress changes the band structure and with it the conductivity of the material. For semiconductors this effect can exceed the others by far. The other two terms take into account the changing geometry due to the stress. The Young's modulus is the material parameter that connects the stress with the strain  $\varepsilon$  ( $\sigma = E \cdot \varepsilon$ ). These changes occur because of the vibration from the structure. When one is calculating the relative change of resistance  $\Delta R/R$  the formula can be rearranged to the "gauge factor" (Eq. 3.3), where the relative change of resistance is related to the strain  $\varepsilon$ . The GF can also be written like in Eq. 3.4, with the advantage that one can see that the PRE has a geometrical  $(1 + 2\nu)$  and a material dependence, with  $\nu$  is the Poisson ratio. The geometrical part shows the same behavior for all kinds of solids like metals and semi-conductors, which comes from thinning. The material part is very different for these groups. As a result the GF is also very different. For metals the GF has a value around  $\sim 1$  to 5 and for semi-conductors around  $\sim 80$  to 200.

$$GF = \frac{\Delta R}{R} \frac{1}{\varepsilon} \quad (3.3)$$

$$GF = \frac{\Delta \rho}{\rho} \frac{1}{\varepsilon} + (1 + 2\nu) \quad (3.4)$$

This big difference is caused by the material effect in semiconductors due to the changed band scheme. In a single crystal silicon the situation is more complicated since the crystal exhibits anisotropic properties. The resistivity is in general a  $3 \times 3$  matrix and also the stress tensor (including normal and shear stress). The piezo resistive parameter between resistivity and stress is consequently a  $3 \times 3 \times 3 \times 3$  tensor with 81-components. Silicon has a cubic crystal symmetry, the matrices are symmetric which allows to write  $\varrho = \varrho_0(1 + \pi_l \cdot \sigma)$  where  $\varrho_0$  is the resistivity under zero stress,  $\pi_l$  the longitudinal piezoresistive coefficient and  $\sigma$  the stress vector. Under zero stress the tensor of resistivity is isotropic and the electric field and the current density is parallel (Riesch [12]). For the resistive material p-doped areas should be implemented into the structure.

#### 3.1.1 Wheatstone Bridge

To measure  $\Delta R/R$  in an effective way the Wheatstone bridge is quite a common setup. As described in [12] the output voltage will be

$$u_d(t) = \frac{1}{2} u_r \pi_l \sigma_l(t) \quad (3.5)$$

with  $u_r$  the readout voltage,  $\pi_l$  the longitudinal piezoresistance coefficient and  $\sigma_l(t)$  the mechanical stress in the piezoresistor. When the sensor is driven with dc voltage  $u_r$  in the resonance frequency, and exciting the vibration with the frequency  $f_e$  the output of the bridge will be

$$u_d = \hat{u}_d \cos(2\pi f_e t + \phi) . \quad (3.6)$$

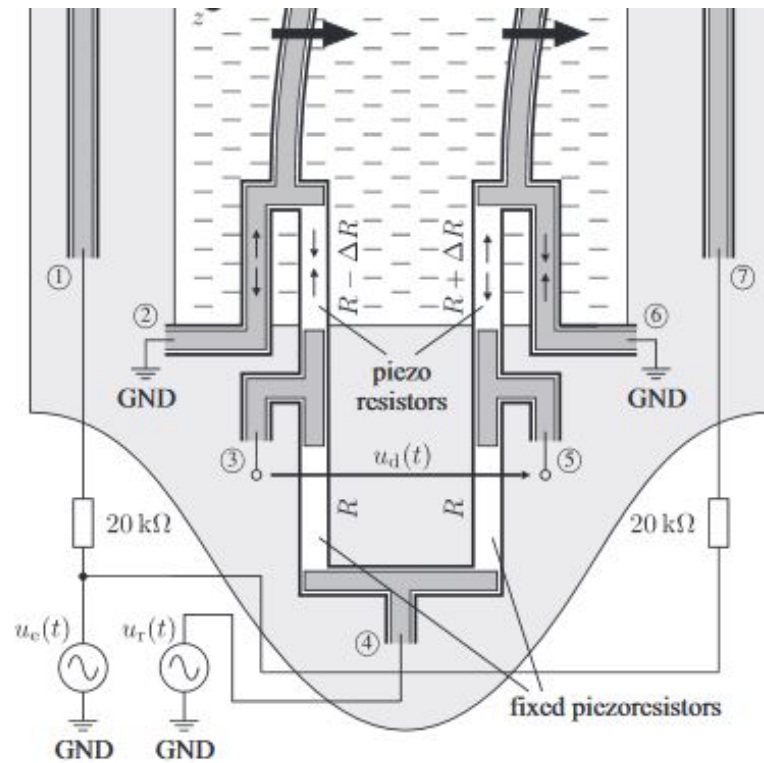
### 3 Readout

Here,  $\phi$  is the phase shift between the excitation and the measured signal. This is possible because the excitation frequency is obviously well-known and the phase shift can be measured with a lock-in amplifier. Unfortunately, the readout of the sensor will be disturbed, due to capacitive, inductive and resistive coupling, with a crosstalk. It is beneficial, if the readout signal (supply voltage of the bridge) is sinusoidal  $u_r = \hat{u}_r \cos(2\pi f_r t)$ , then the output voltage  $u_d$  will be

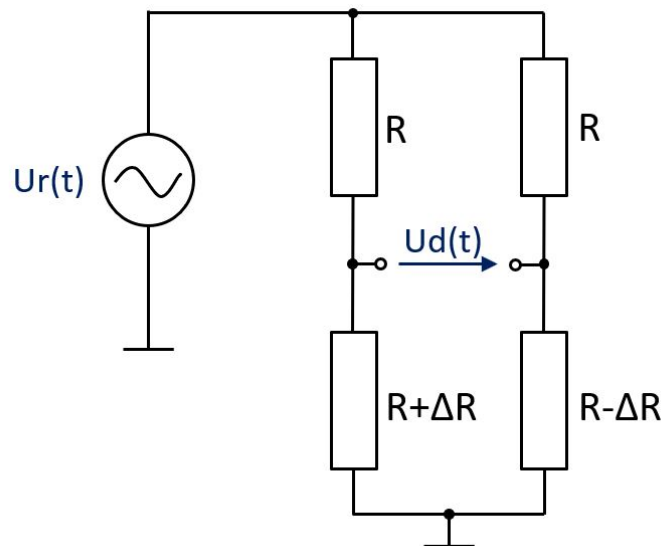
$$u_d(t) = \frac{1}{2} \pi_l \hat{u}_r \cos(2\pi f_r t) \hat{\sigma}_l \cos(2\pi f_e + \phi) \quad (3.7)$$

$$u_d(t) = \frac{1}{4} \pi_l \hat{u}_r \hat{\sigma}_l \{ \cos[2\pi(f_r - f_e)t - \phi] + \cos[2\pi(f_r + f_e)t - \phi] \} \quad (3.8)$$

When the lock-in amplifier is set to either  $|f_r - f_e|$  or  $|f_r + f_e|$  the signal can be measured without any crosstalk. In Fig. 3.1a one can see a half Wheatstone bridge where two piezo-resistive regions are fixed and two will change during the vibration of the structure. The piezo resistors are build with p-doped regions of the silicon. For an easier understanding the readout part of Fig. 3.1a is transferred to a schematic circuit in Fig. 3.1b. Here, one can see that the lower part must be on the vibrating structure and that the resistor change must be antisymmetrical in order to get the output voltage  $u_d(t)$ .



(a) Readout with the Wheatstone bridge on the sensor structure, with a readout and excitation circuit. [12].



(b) Schematic of the Wheatstone bridge, the fixed resistors are on the Si-frame would not be on the moving part of the structure, the resistors with a  $\Delta R$  part are on the vibrating beam.

Figure 3.1: Schematic of the Wheatstone bridge.

## 3.2 Optical Readout

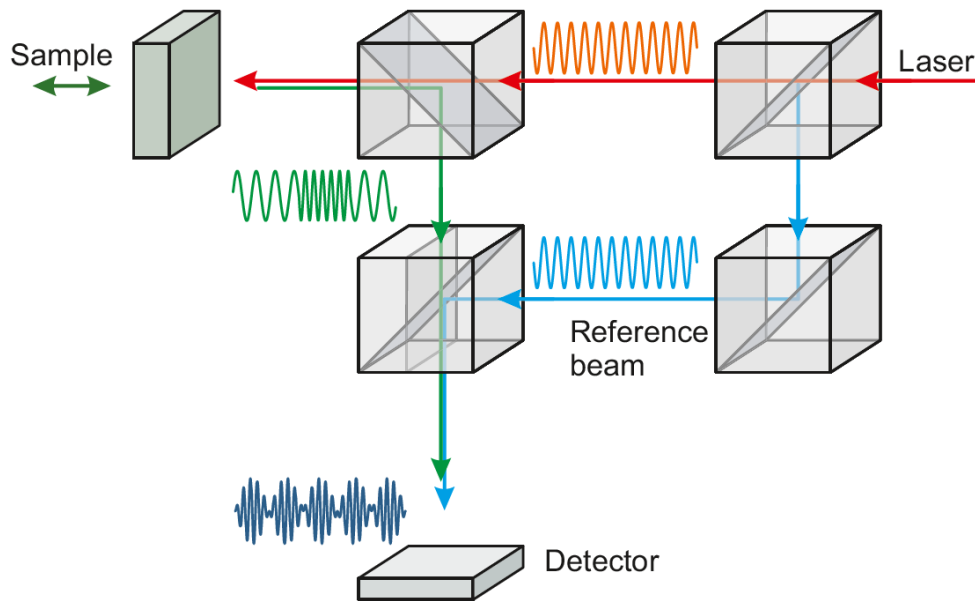
For the optical readout the ISAS has an MSA (Micro System Analyzer), which is a laser Doppler vibrometer for miniaturized structures (LDV) and that is introduced in the following. Here a laser beam is split into two beams, as depicted in Fig. 3.2a. While the reference beam has no obstacle in the way rather than mirrors, the other laser beam is reflected on the measured object. When reflected on this moving object, like a vibrating sensor structure, as it is the case for this thesis, the frequency of the laser beam changes. This is described through the Doppler effect, which can be observed two times in this measurement setup, first time when the laser beam is hitting the moving object and the second time when the laser beam is emitted by the moving object to the stationary MSA. These cases are depicted in Fig. 3.2b and Fig. 3.2c. The summarizing effects can also be calculated with

$$f_{E2} = f_{Q1} \frac{1 - \frac{\vec{v} \cdot \vec{e}_1}{c}}{1 - \frac{\vec{v} \cdot \vec{e}_2}{c}} \quad (3.9)$$

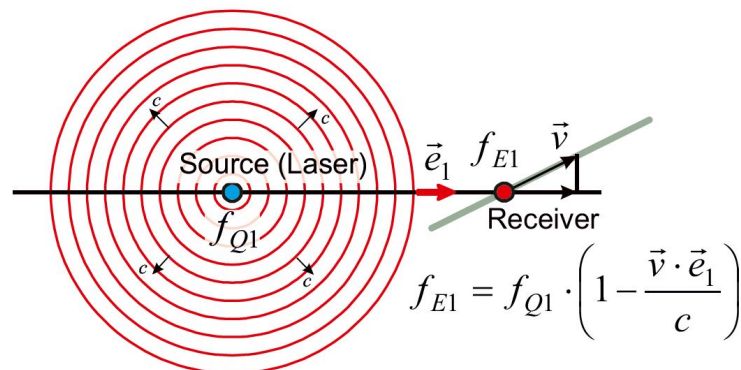
with  $f_{E2}$  the reflected and  $f_{Q1}$  the incoming laser beam,  $c$  the velocity of light,  $\vec{v}$  the velocity of the moving object,  $\vec{e}_1$  and  $\vec{e}_2$  the direction between source and receiver of the laser beam. The difference between the frequency at from the source and after reflection at the receiver is  $f_D = f_{Q1} - f_{E2}$  heads to

$$f_D = v \cdot \frac{2}{\lambda} \quad (3.10)$$

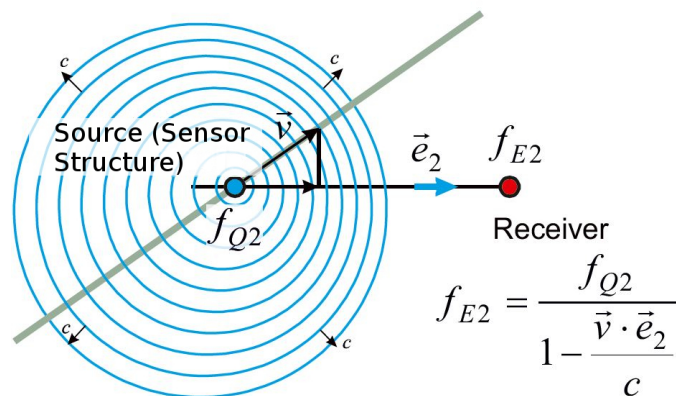
and can be measured through interference with the reference beam at the detector. It reveals that frequency is proportional to the velocity of the moving measurement object and the wavelength of the laser beam. At the MSA this measurement principle is performed on several predefined positions on the structure, while a signal from the MSA brings the resonator through the Lorentz force into vibration. The velocity of this vibration is measured and through analyzing of the data one can see all the excited eigenmodes.



(a) Function principle of the MSA.  
Stationary Source - Moving Observer



(b) Doppler effect for stationary source (MSA) and moving receiver (sensor structure).  
Moving Source - Stationary Observer



(c) Doppler effect for moving source (sensor structure) and stationary receiver (MSA).

Figure 3.2: The Doppler effect used for the MSA.

### 3.3 Piezoelectric Layer Readout

A piezoelectric layer readout would have the biggest advantages, since it can be used for the readout and excitation in the same way. Here the principle of charge deforming the material is used, as described by Schmid [13]. On the one hand the structures vibration would induce charge that could be measured with the electric field, on the other hand an external electric field will modify the material, this deformation could be used to excite the structure. However, a piezoelectric layer would be another complicated technological step, so it was put aside for this thesis, but the benefits of piezoelectric or even ferro-electrics material could be enormous.

## 4 Excitation

The structure needs to be excited in order to vibrate at the resonance. There are some possibilities for doing so, like thermoelastical, electrostatical, electrodynamical, piezoelectrical (or ferroelectric) and with nanostructures even optical ones. The piezoelectric actuation would have the biggest benefit, because the same layer could excite and sense at the same time. The process of implementing such a layer is very difficult, so two other principles were considered for this thesis.

### 4.1 Lorentz force

The electromagnetic principle is very common and especially handy for prototypes, since one only needs an external magnetic field and to sputter a conductive material onto the vibrating structure to form a lead. In most cases a permanent magnet is used, but electromagnets are possible as well. As stated in Schmid [13], with the Halbach array magnetic flux density up to 2 T are possible. The force behind this principle is the Lorentz force and (homogeneous) magnetic fields.

$$\vec{F}_L = I \vec{L} \times \vec{B} \quad (4.1)$$

An AC current flows over the structure and a magnetic field normal to the current flow will excite the structure in a certain mode. For this thesis the magnet needs to be under the structure, so the in-plane mode can be excited. Note that with the Lorentz force only odd modes can be excited, since the force is symmetric in the even modes so

#### 4 Excitation

that the structure would not vibrate. For the excitation of even modes inhomogeneous fields would be required.

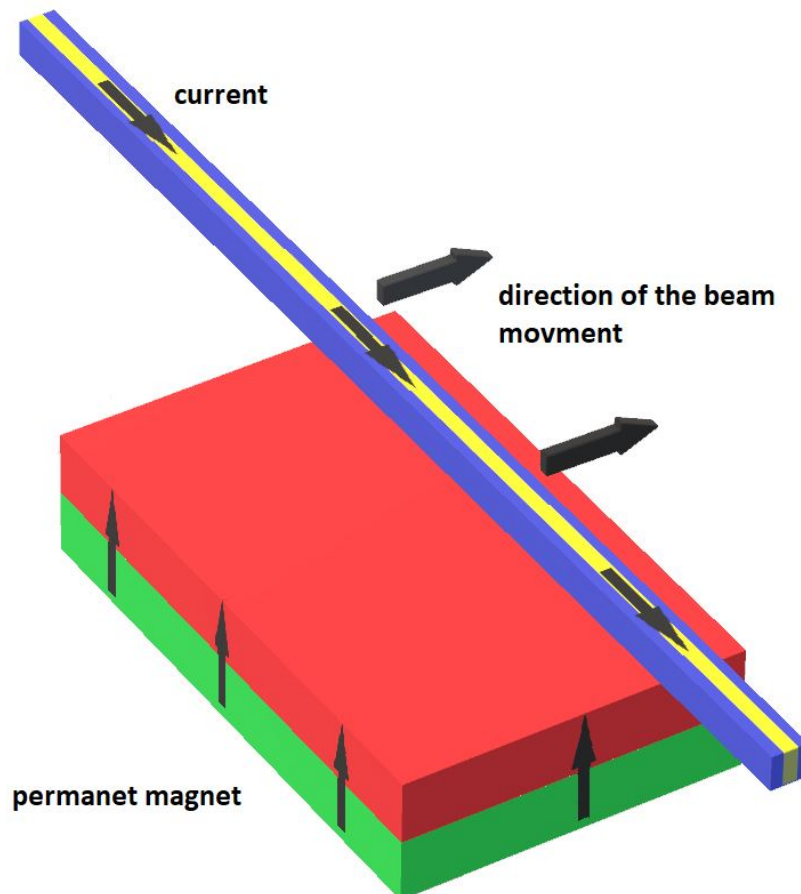


**Figure 4.1:** Sketch of a beam of the actuation principle for this thesis. The permanent magnet has a flux density in the upper direction. The current will be alternating, therefore, the beam moves in the respective direction. The movement direction results from Eq. 4.1.

## 4.2 Piezo-electric

This principle is also quite simple and shown in Fig. 4.2. A piezoelectric crystal is positioned in a certain way to excite the structure while it oscillates in its resonance frequency. The crystal is in contact with the structure and excites it directly. The crystal, as they are available for different frequency ranges, needs to swing in the same direction as the desired direction of the sensor.

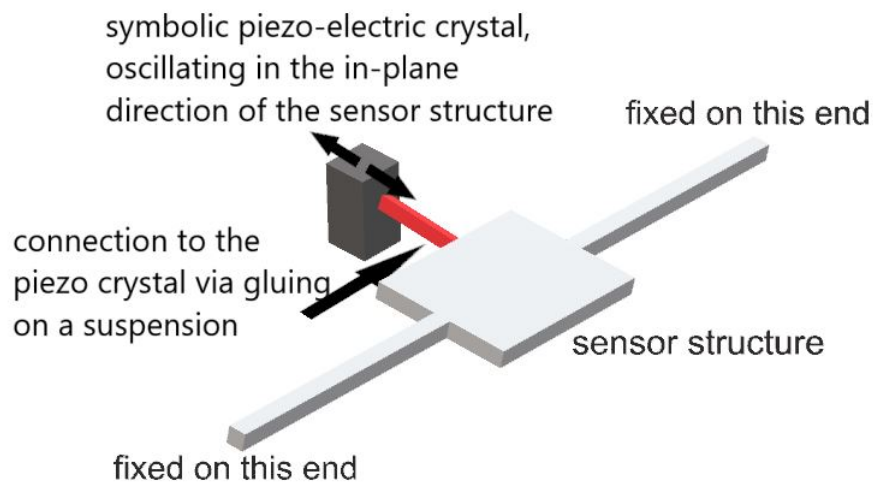


Figure 4.2: Basic principle of the piezo-electric actuation.



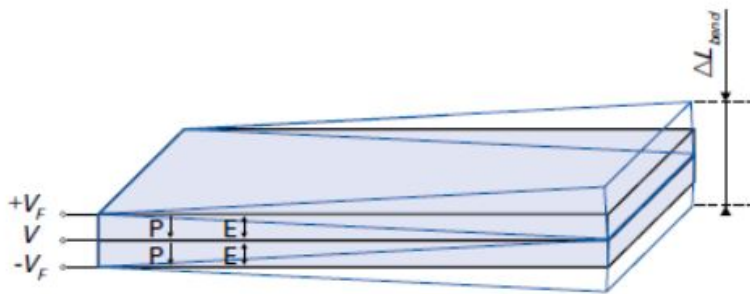
## 5 Measurement

Beside the possible improvement of the design and the selection of a read out and actuation method the validation sensor principle is important for this thesis. Below one can find the description of the measurement setup and the results from first measurements.

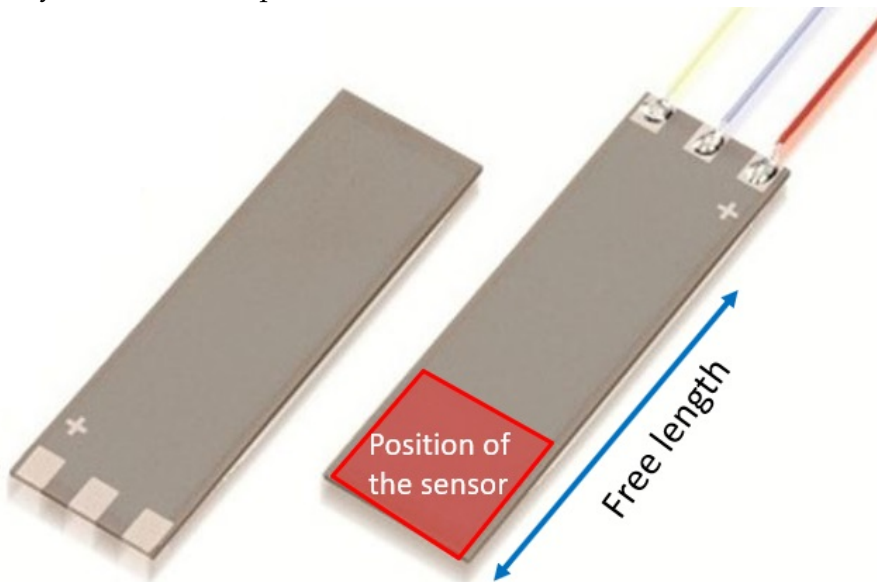
### 5.1 Measurement Setup

The idea was to achieve a displacement similar to the simulated conditions 2.2, therefore, a special bending actuator was used, as depict in Fig. 5.1b. This allows to bend the sensor structure like implemented in a cantilever of an AFM. When the supply voltage of the actor is bipolar ( $-30\text{ V}$  and  $30\text{ V}$ ) it is possible to deflect the bow actor at the end into both directions by about  $\pm 100\text{ }\mu\text{m}$ . For the measurement two DC sources are required, one for the supply and one for the control voltage, which is needed to adjust the deflection. In picture 5.2 one can see the measurement setup, with the mounted sensor, actuation circuit, magnets and part of the optical system of the MSA.

## 5 Measurement



- (a) The bending actuator has thin piezoceramic layers and internal electrodes. If the voltage is applied correctly the layers expand and the length contracts, caused by the  $d_{31}$  effect. This results in a bending movement, hence, displacement as desired.  $V_F$  is here the supply voltage,  $V$  the control voltage,  $P$  and  $E$  are the polarization and electrical field, respectively, and  $\Delta L$  the displacement.



- (b) The sensor has to be positioned at the free length of the bending actuator, to guarantee the maximum possible bending movement. Furthermore, the sensor has to be fixed to the edge, as indicated with the red square, to achieve the largest displacement. The wires are connected to the supply and control voltage sources.

Figure 5.1: Bending actor [6]

### 5.1.1 Fixing to the Actor

An epoxy resin was used to fix the sensor onto the actuator. It is important to glue the sensor close to the edge as sketched in Fig. 5.1b. If the sensor is glued out of the free length, the actuator cannot deflect the whole range of  $\pm 100 \mu\text{m}$ . After gluing, the sensor was connected via gold bond wires (hardly visibly in Fig. 5.3) to the PCB. As there is no further packaging in this development stage, the bond wires had to be handled very carefully.

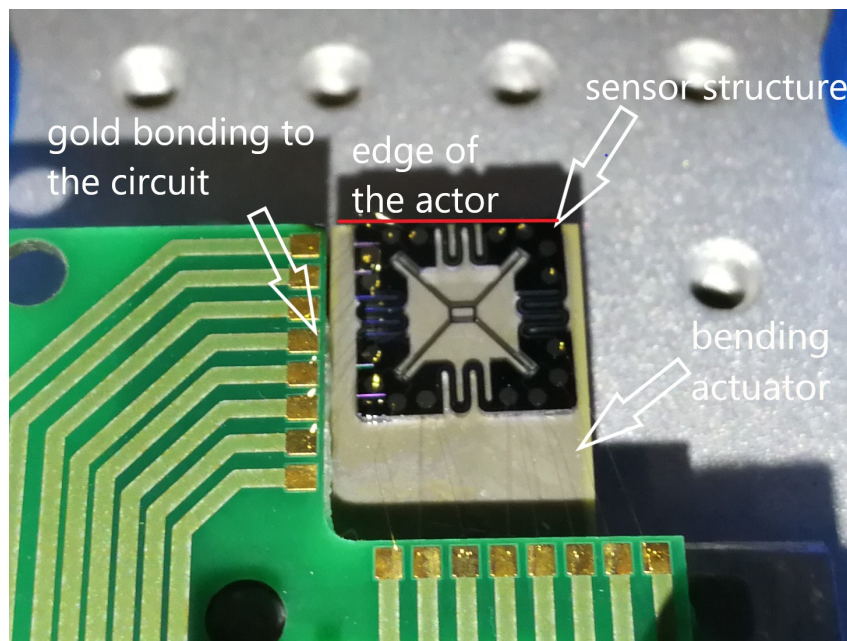


**Figure 5.3:** Detailed picture of the sensor on the bending actuator. One can see that the sensor is glued to the edge (red line), so the actor can deflect completely. Hardly visible is the gold bonding to the circuit, which generates the current to bring the structure in vibration through the Lorentz force.

## 5 Measurement

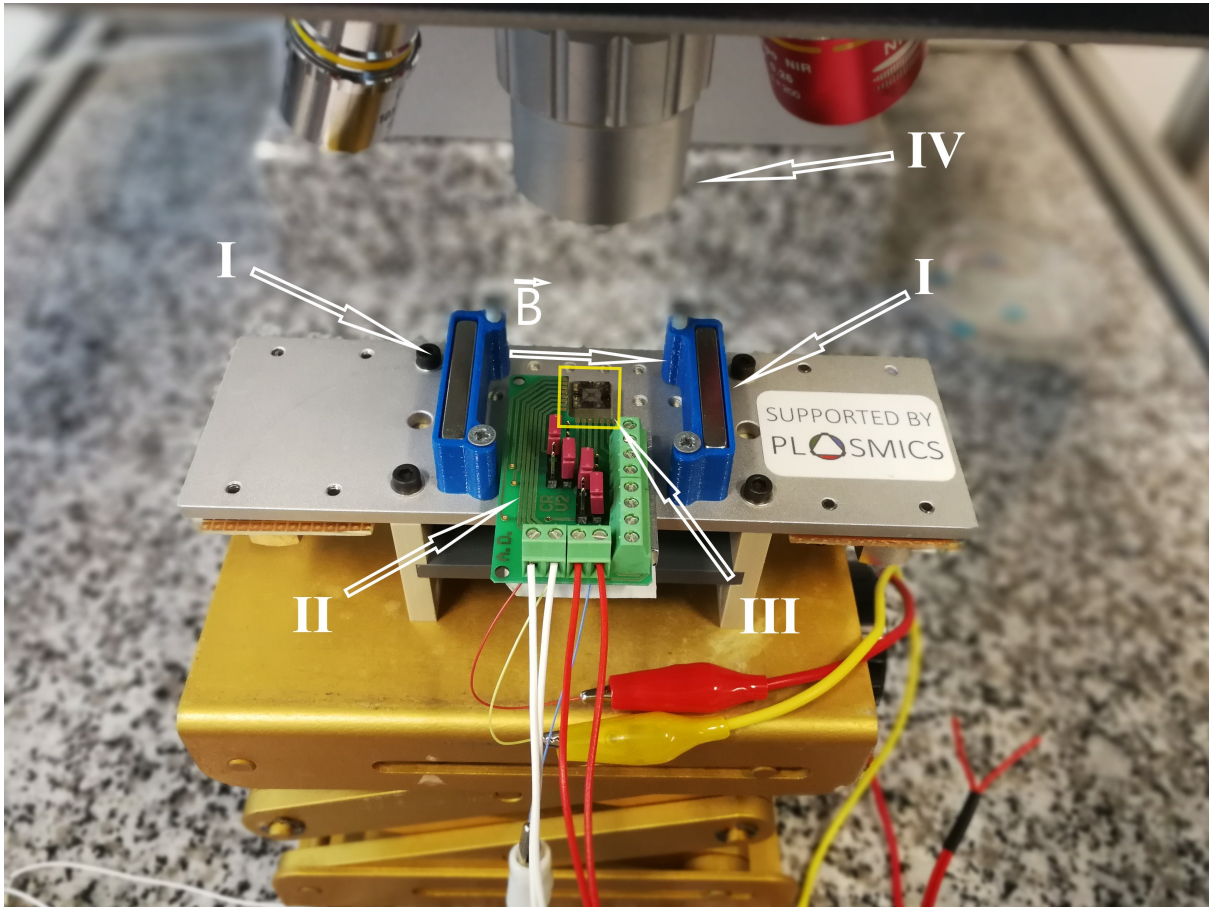


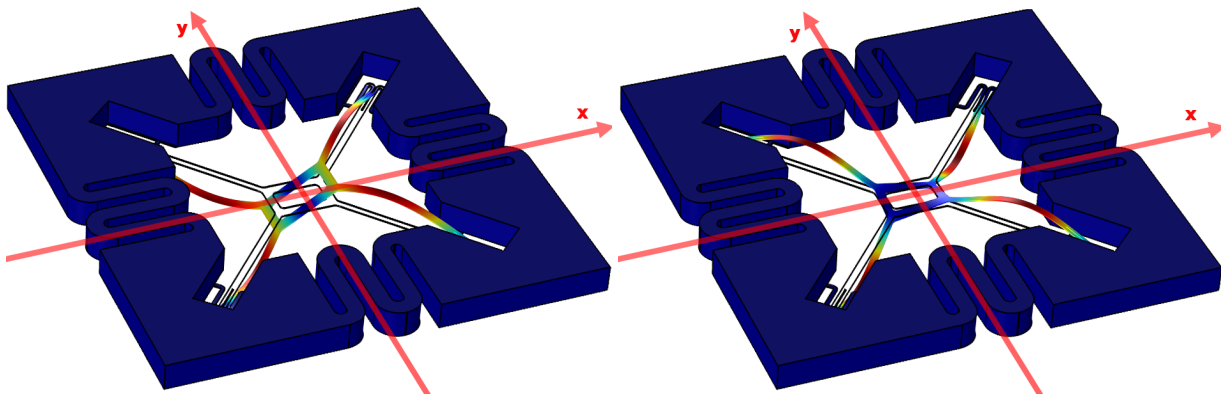
**Figure 5.2:** Measurement setup I: Permanent magnets for the external magnetic field, with B-field direction as marked. II: Circuit with gold bonding for the excitation signal. III: MEMS sensor. IV: Optic of the MSA. The yellow square marks a cutout of the figure, which is depicted enhanced in Fig. 5.3. Here, one can see the sensor fixed to the edge of the bending actuator.

## 5.2 Results

In the measurements two modes, the first symmetrical and the first antisymmetric, were investigated (Fig. 5.6). For the deflection of the actor the control signal was always changed about 1 V, which relates to a 2  $\mu\text{m}$  large displacement on the sensor. In order to get reliable results the measurements were repeated multiple times in the range from 20 V to  $-20$  V, therefore, yielding a displacement of 40  $\mu\text{m}$  to  $-40$   $\mu\text{m}$ . In Fig. 5.4 one can see the results from the first symmetric mode, an out-of-plane mode. Without any displacement the sensor has a higher frequency and the frequency is reduced when the actor bends in negative direction. This is surprising, but can be explained with a prestress in the structure caused by the gluing. When the bow actor bends into the negative direction this prestress is reduced. Through comparison with the simulated data one can imply that the structure has a prestress like it is bent 40  $\mu\text{m}$  in the positive direction, this is also the offset for the simulated data to compare the FEM and measured data in Fig. 5.4. The points in the measurement curve are the averaged of 8 measurements, the bars represent the standard deviation. Around  $U_C = -10$  V to 0 V the measured data has a slope of 0.142 kHz/V, which corresponds to a responsivity of 70 Hz/ $\mu\text{m}$ . Very satisfying is the fact that the simulation fits so well with the measurements, as one can see in Fig. 5.4. The simulated values appear nearly all next to the measured values and are linear. The difference could be caused by another kind of displacement. In the simulation the displacement is a boundary condition on the edge of the structure (like it is described in chapter 2.2), but in the measurement the displacement actor has a bending which acts on the bottom, the gluing area, of the sensor. The nonlinearity can be caused by the gluing material, as the epoxy resin will absorb some of the mechanical stress. An indication for this is that the nonlinearity seems to be only in the range with the negative deflection of the structure, which is the range where the prestress caused by the glue is reduced. The second investigated mode was the first antisymmetric mode, this would be the fifth simulated mode. Here, the slope is about the factor ten smaller than of the first symmetric mode, which corresponds to a responsivity of 7 Hz/ $\mu\text{m}$ . Unfortunately, the deviation between

## 5 Measurement

simulation and measurement is with 15 kHz rather high, hence the curves were not depicted. This effect is not uncommon as the simulation of higher modes exhibit usually larger errors. There is also an unexpected behavior near  $U_C = 0$  V. This effect occurred when the supply voltage was switched from positive to a negative voltage, although this effect could not be observed at the first symmetrical mode. This effect would require a more detailed investigation, but this would be beyond the scope of this thesis. Also very interesting is the range  $U_C = -15$  V to  $U_C = -20$  V, here the resonance frequency rises again. This is clearly a sign that the prestress is completely reduced and the stress rises again. An effect that was already expected in the in the range below  $U_C = 0$  V.



- (a) Side view of the first SA mode. It is symmetrical to the y-axis and antisymmetrical to the x-axis, therefore, called symmetrical mode in this thesis.
- (b) Side view of the first AA mode. It is antisymmetrical to the y-axis and antisymmetrical to the x-axis, therefore, called antisymmetrical mode in this thesis.

Figure 5.6: Modeshape in COMSOL for the measurement

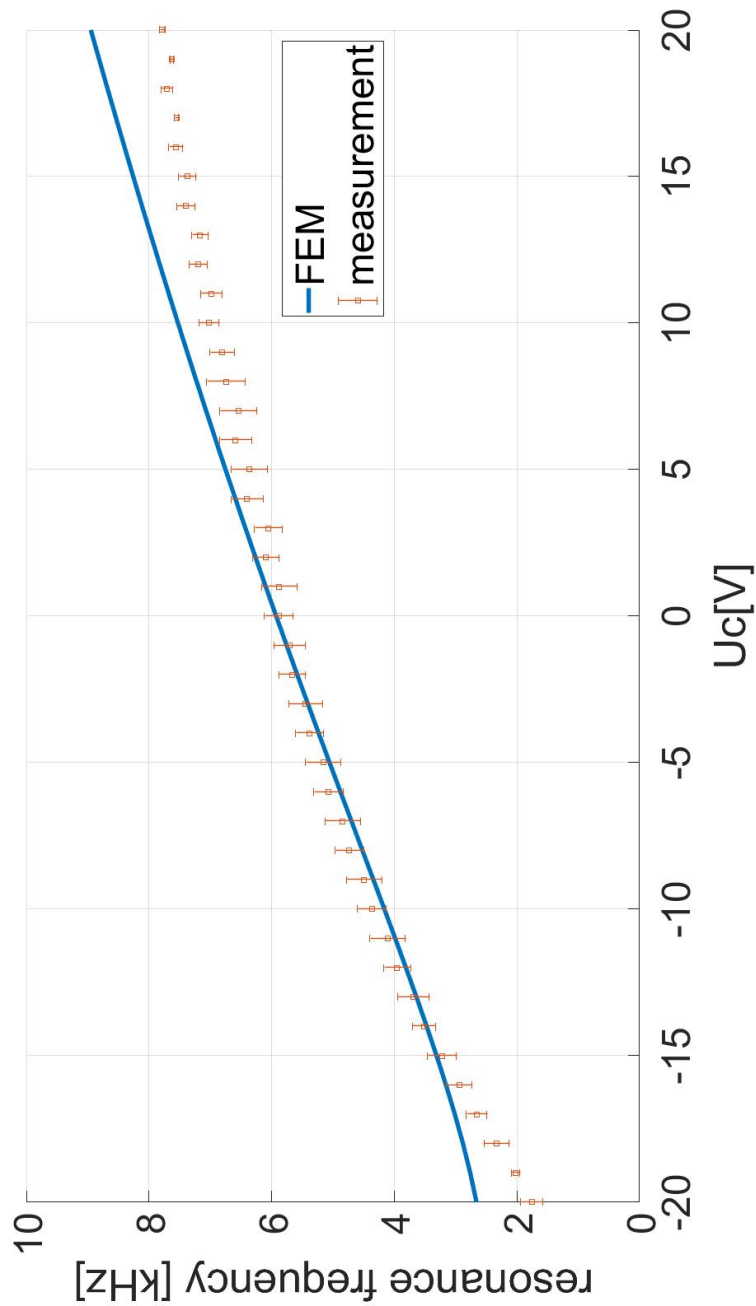


Figure 5.4: Measurement result of the first symmetric mode, the slope  $70 \text{ Hz}/\mu\text{m}$  on average. The simulation data has an offset of  $-40 \mu\text{m}$  to compensate the prestress of the measured values and make the data comparable. The control voltage  $U_C$  adjusts the deflection of the actor, with this setup,  $\Delta U_C = 1 \text{ V}$  relates to a displacement of  $2 \mu\text{m}$  on the structure.

## 5 Measurement

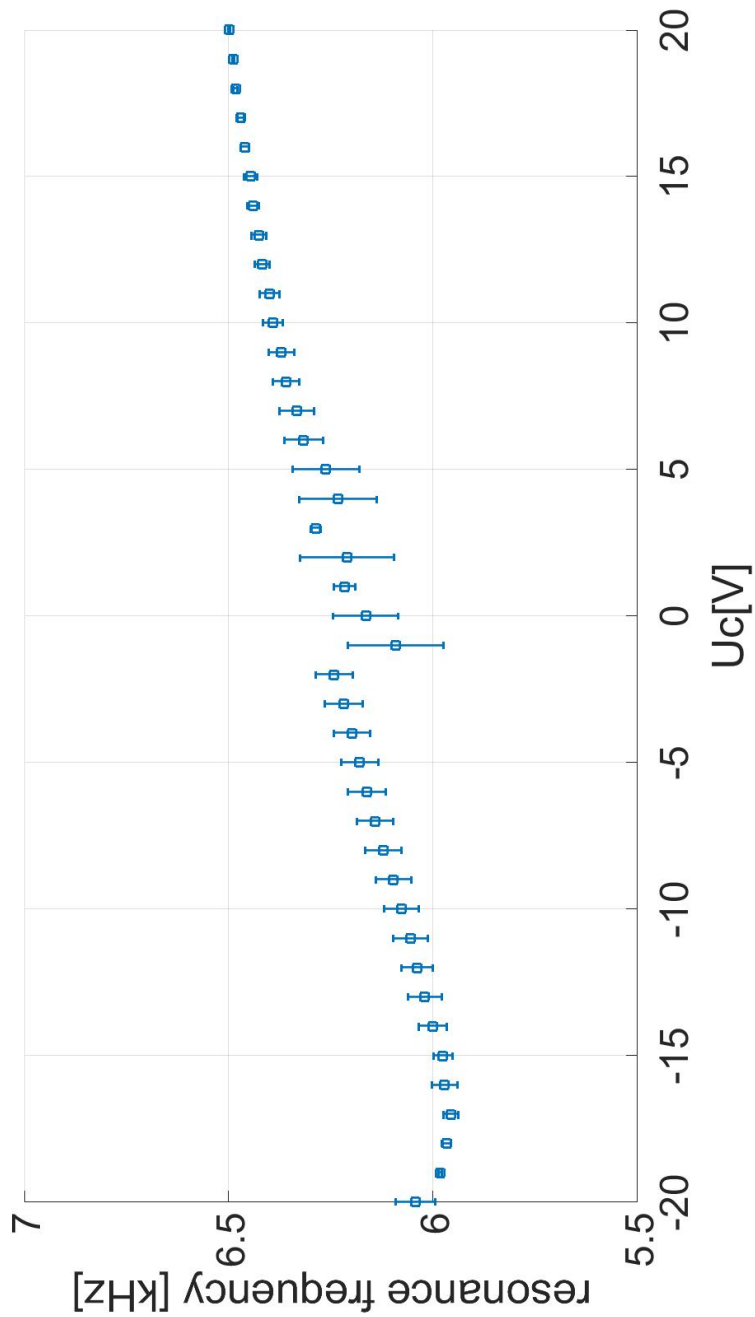


Figure 5.5: Measurement result of the first antisymmetrical mode (fifth harmonic), the slope is 0.0144 kHz/V on average, which relates to 7 Hz/ $\mu\text{m}$ . At the range below  $U_C = -15$  V the prestress is completely reduced and the eigenfrequency rises again. The control voltage  $U_C$  adjusts the deflection of the actor, with this setup,  $\Delta U_C = 1$  V relates to a displacement of 2  $\mu\text{m}$  on the structure.

## 6 Conclusion

First of all, the thesis shows that MEMS sensors with a displacement out of the plane can be exactly simulated with a FEM software and that the simulations confirmed the measurement results. It is also possible to calculate the eigenfrequency change caused by geometrical modification with a simple reduced analytical model. The deviation between these models was less than seven percent.

For achieving a very small sensitivity the dimensions of the sensor and mechanical stress on the structure are crucial. The disadvantage of increasing the beam length to get a soft resonator is limited, since this parameter can easily increase the responsivity but it decreases the resonance frequency as well. The ratio between beam length and thickness or width that should undercut 0.1, as the simulations showed. A potential for improvement is also found in the material: a higher Young's modulus (as for SiC), for instance, would increase the sensors rigidity and reduce the displacement for a fixed mechanical load, but if the displacement is fixed on the other hand and the mechanical load is negligible, the responsivity would be higher and the disadvantage can be passed. The impact of a change in thickness and width depends on the direction in which the mode shape vibrates. For an in-plane mode a change of the beam width has a strong effect, while a change of the thickness barely changes anything. For the out-of-plane mode the same can be stated but for exchanged parameters width and height. Furthermore, unnecessary mass should be reduced to get a higher resonance frequency as the analytical and FEM simulation showed. This can be achieved by other materials or designs. The use of multiple beams with the effect of SCR can be an easy way to increase the eigenfrequency of the structure.

## 6 Conclusion

The measurement of the alternative sensor could confirm the simulation of this thesis, at the first mode there was a small deviation between simulation and measurement. Although the simulation could be approximated as linear in this region, the measurement was nonlinear. This can be caused by the difference between real and simulated displacement, the glue under the sensor or by the linearity of the displacement actor itself. Nonetheless the sensor behavior was satisfying as it seems that most part of the error results from the measurement setup. The integration of the new designed sensor structure with its high responsivity, into other systems like an AFM cantilever could improve the system a lot. Although the excitation with an external magnetic field needs some innovation, technology like piezo- or ferroelectric layers may be a solution.

## Bibliography

- [1] Reza Abdolvand. *Micromachined Resonators: A Review*. 2016 (cit. on p. 4).
- [2] Cagatay Basdogan Bilal Orun Serkan Necipoglu and Levent Guvenc. *State Feedback Control for Adjusting the Dynamic Behavior of a Piezo-actuated Bimorph AFM Probe*. 2006 (cit. on p. 4).
- [3] Alexander Dabsch. *A Sensor in a Nutshell*. 2018 (cit. on pp. 35, 36).
- [4] Alexander Dabsch. *Multiaxial Resonant MEMS Force Sensor*. 2017 (cit. on pp. 15, 16).
- [5] Zhanshe Gui and Buyi Li. "Theory and experimental research for the double ended tuning fork in MEMS." In: *Emerald* (2015) (cit. on p. 25).
- [6] Website Physik Instrumente, ed. 2019 (cit. on p. 50).
- [7] Helga Dankert Juergen Dankert. *Technische Mechanik*. 2013. Chap. 32 (cit. on pp. 6, 9, 12).
- [8] K. Kalantar-zadeh. *Sensors*. 2013 (cit. on p. 2).
- [9] Franz Keplinger. *Sensorik*. 2017. Chap. 3 (cit. on p. 1).
- [10] Isabella Dufour Oliver Brand. *Resonant MEMS*. 2015 (cit. on p. 1).
- [11] Rubén Pérez. *Dynamic Atomic Force Microscopy: Basic Concepts*. 2012 (cit. on pp. 2, 20).
- [12] Christina Riesch. *Micromachined Viscosity Sensors*. 2009 (cit. on pp. 39, 41).
- [13] Silvan Schmid. *Fundamentals of Nanomechanical Resonators*. 2016 (cit. on pp. 2–4, 15, 20, 26, 38, 44, 45).

## Bibliography

- [14] Husna Omar Sh Mohd Firdaus and Ishak Abd Azid. *High Sensitive Piezoresistive Cantilever MEMS Based Sensor by Introducing Stress Concentration Region (SCR)*. 2012 (cit. on pp. 20, 26).
- [15] Shenjie Zhou Shengli Kong. "The size-dependent natural frequency of Bernoulli–Euler micro-beams." In: *ScienceDirect* (2007) (cit. on pp. 9, 22–24).